Monthly Notices of the ROYAL ASTRONOMICAL SOCIETY

MNRAS **519,** 709–728 (2023)
Advance Access publication 2022 November 28

https://doi.org/10.1093/mnras/stac3486

The nature of 500 micron risers – II. Multiplicities and environments of sub-mm faint dusty star-forming galaxies

J. Cairns,[1]★ D. L. Clements,[1] J. Greenslade,[1] G. Petitpas,[2] T. Cheng,[1] Y. Ding,[1] A. Parmar,[1] I. Pérez-Fournon[3,4] and D. Riechers[5]

[1]*Imperial College London, Blackett Laboratory, Prince Consort Road, London SW7 2AZ, UK*
[2]*Harvard-Smithsonian Center for Astrophysics, 60 Garden Street, Cambridge, MA 02138, USA*
[3]*Instituto de Astrofísica de Canarias, C/Vía Láctea, s/n, E-38205 San Cristóbal de La Laguna, Tenerife, Spain*
[4]*Dpto. Astrofísica, Universidad de La Laguna, E-38206 San Cristóbal de La Laguna, Tenerife, Spain*
[5]*I. Physikalisches Institut, Universität zu Köln, Zülpicher Strasse 77, D-50937 Köln, Germany*

Accepted 2022 November 18. Received 2022 November 17; in original form 2022 February 26

ABSTRACT

We present Submillimeter Common User Bolometer Array 2 (SCUBA-2) and Submillimeter Array (SMA) follow-up observations of four candidate high-redshift dusty star-forming galaxies, selected as sources with rising spectral energy distributions in the 250, 350, and 500 μm *Herschel* SPIRE bands. Previous SMA observations showed no counterparts to these sources, but in our deeper sub-mm observations we detect counterparts to all four 500 μm risers, with three resolving into multiple systems. For these three multiple systems, the SMA 345 GHz (≈870 μm) observations recover 123 ± 73 per cent, 60 ± 15 per cent, and 19 ± 4 per cent of the integrated 850 μm flux density from SCUBA-2, indicating that there may be additional sources below our SMA detection limit making up a dense, protocluster core. The fourth 500 μm riser was observed at a lower frequency and so we cannot make a similar comparison. We estimate photometric redshifts based on FIR/sub-mm colours, finding that three fourths likely lie at $z \geq 2$. This fits with the interpretation that the 500 μm riser selection criterion selects both intrinsically red, individual galaxies at $z > 4$, and multiple systems at more moderate redshifts, artificially reddened by the effects of blending. We use the SCUBA-2 850 μm maps to investigate the environments of these 500 μm risers. By constructing cumulative number counts and estimating photometric redshifts for surrounding SCUBA-2 detections, we find that one of our 500 μm risers could plausibly reside in a $z \geq 2$ protocluster. We infer that bright 500 μm risers with faint 850 μm flux densities are typically multiple systems at $z \geq 2$ that may reside in overdensities of bright sub-mm galaxies.

Key words: galaxies: high-redshift – galaxies: starburst – infrared: galaxies – submillimetre: galaxies.

1 INTRODUCTION

Dusty star-forming galaxies (DSFGs) provide an enormous contribution to the total energy density emitted by galaxies and hence represent a vital stage in their formation and evolution. In the last couple of decades, there has been a profound development in our understanding of the nature of DSFGs and their role in galaxy formation and evolution, particularly those selected at sub-mm wavelengths (typically 850 μm). These sources have subsequently come to be known as sub-mm galaxies (SMGs; Blain et al. 2002), and were first detected and characterized using the Submillimeter Common User Bolometer Array (SCUBA: Cunningham et al. 1994) on the James Clerk Maxwell Telescope (JCMT) prior to the turn of the century (Smail, Ivison & Blain 1997; Barger et al. 1998; Hughes et al. 1998). The redshift distribution of SMGs peaks at $z \sim 2$–3 with a significant tail extending to higher redshifts (Chapman et al. 2005; Wardlow et al. 2011; Koprowski et al. 2014; Simpson et al. 2014; Danielson et al. 2017; Smith et al. 2017; Stach et al. 2019). SMGs are typically massive ($M_\star \sim 10^{10}$–10^{11} $M_\odot$: Swinbank et al. 2004; Hainline et al. 2011; Michałowski et al. 2012; Gruppioni et al. 2013; Simpson et al. 2014; Dudzevičiūtė et al. 2020; Pantoni et al. 2021), rich in both gas and dust (Smail et al. 2002; Greve et al. 2005; Kovács et al. 2006; Tacconi et al. 2006, 2008; Carilli et al. 2010; Clements, Dunne & Eales 2010; Bothwell et al. 2013; Dudzevičiūtė et al. 2020; Pantoni et al. 2021), and extremely luminous, with total infrared luminosities of $L_{\rm IR} \sim 10^{11}$–10^{13} $L_\odot$ (Chapman et al. 2005; Magnelli et al. 2012; Swinbank et al. 2014; Gruppioni et al. 2015; MacKenzie et al. 2017; Michałowski et al. 2017; Hill et al. 2018; Rowan-Robinson et al. 2018; Cheng et al. 2019; Greenslade et al. 2020), corresponding to dust-obscured star formation rates (SFRs) of hundreds to thousands of solar masses per year, contributing significantly to the Cosmic Star Formation Rate Density (CSFRD) at these redshifts (Chapman et al. 2005; Wardlow et al. 2011; Barger et al. 2012; Swinbank et al. 2014; Smith et al. 2017; Dudzevičiūtė et al. 2020). There is still debate surrounding the morphology and origin of DSFGs and they are likely a diverse population in this respect (see e.g. Casey, Narayanan & Cooray 2014). Some suggest that many DSFGs may represent isolated, gas-rich, disc galaxies undergoing a burst of star formation (Carilli et al. 2010; Davé et al. 2010; Targett et al. 2013; Michałowski et al. 2017), while others suggest that they are primarily merger-driven (Baugh et al. 2005;

★ E-mail: j.cairns18@imperial.ac.uk

© 2022 The Author(s)
Published by Oxford University Press on behalf of Royal Astronomical Society

Downloaded from academic.oup.com/mnras/article/519/1/709/6849985 by Imperial College of Science Technology and Medicine user on 19 October 2026

Tacconi et al. 2008; Engel et al. 2010; Ivison et al. 2012; Kartaltepe et al. 2012; Chen et al. 2015; Cochrane et al. 2021) and potentially represent a key, short-lived (typically of order a few hundred Myr: Casey 2016; Pantoni et al. 2021) phase in an evolutionary sequence, followed by a bright quasar phase which decays, leaving a massive elliptical galaxy (Alexander et al. 2005; Farrah et al. 2006; Hopkins et al. 2008; Cook et al. 2010; Toft et al. 2014; Wilkinson et al. 2017; Dudzevičiūtė et al. 2020). While SMGs are important objects to study in their own right, a number of studies have found numerous DSFGs lying within high-redshift protoclusters (Daddi et al. 2009; Capak et al. 2011; Walter et al. 2012; Clements et al. 2014, 2016; Dannerbauer et al. 2014; Casey et al. 2015; Umehata et al. 2015; Wang et al. 2016; Greenslade et al. 2018; Miller et al. 2018; Oteo et al. 2018; Gómez-Guijarro et al. 2019; Kneissl et al. 2019; Álvarez Crespo et al. 2021; Jones et al. 2021; Wang et al. 2021), thought to be the progenitors of local, massive galaxy clusters. SMGs therefore have the potential to be signposts for overdense regions in the early Universe, whose study can be used to test cosmological models and investigate the formation and evolution of large-scale structure (see e.g. Marrone et al. 2018).

Despite this progress, our understanding of the nature of SMGs remains incomplete, particularly at $z > 4$ where small samples and a lack of spectroscopic confirmations obstructs further progress. The *Herschel Space Observatory* discovered a surprisingly large population ($3.3 \pm 0.8\,\mathrm{deg}^{-2}$) of extremely luminous candidate $z > 4$ DSFGs, selected as sources with a rising spectral energy distribution (SED) in the three *Herschel* SPIRE (Griffin et al. 2010) bands (i.e. $S_{250} < S_{350} < S_{500}$: Dowell et al. 2014; Asboth et al. 2016; Ivison et al. 2016), known as '500 μm risers'. Numerous 500 μm risers have been confirmed at $z > 4$ (e.g. Cox et al. 2011; Riechers et al. 2013, 2017, 2021; Fudamoto et al. 2017) with corresponding SFRs in excess of $1000\,\mathrm{M}_{\odot}\,\mathrm{yr}^{-1}$, making them extreme objects, potentially at the high-luminosity end of a larger population of high-z DSFGs (Greenslade et al. 2020). Simulations have significant difficulty reproducing this population while simultaneously satisfying other observational constraints (see e.g. Hayward et al. 2021, and references therein). Accumulating observations of high-redshift DSFGs is therefore crucial for a complete understanding of this population. Very few studies have focused on investigating the nature of these 500 μm risers, and as such the majority of their properties remain poorly constrained. Simulations suggest that ∼40 per cent of faint ($S_{500} < 60$ mJy) *Herschel* sources should be comprised of multiple DSFGs, while the brightest should be exclusively strongly lensed single galaxies (Béthermin et al. 2017). Some fraction of these multiple systems will be chance line-of-sight alignments of DSFGs, rather than physically associated structures. Oteo et al. (2017) provide follow-up observations of a sample of 44 500 μm risers with the Atacama Large Millimeter Array (ALMA: Brown, Wild & Cunningham 2004), finding that ∼61 per cent resolve into a single sub-mm bright source, while the remainder break up into multiple DSFGs (four break up into ≥3 sources, with one resolving into five separate sources in the synthesized ∼0.12 arcsec ALMA beam). Additionally, 18 of their sources show evidence of gravitational lensing. Greenslade et al. (2020), hereafter known as G20, selected a sample of 34 500-μm risers from the *Herschel* Multi-tiered Extragalactic Survey (HerMES: Oliver et al. 2012), and carried out interferometric follow-up observations with the Submillimeter Array (SMA: Ho, Moran & Lo 2004) between 2010 and 2015. They found that four break up into two individual sources and 18 resolve into a single source, with the remaining 12 maps containing no apparent SMA counterpart. G20 suggested that non-detections were likely a result of the bright *Herschel* sources breaking up into multiple faint counterparts clustered within the *Herschel* SPIRE beamsize (∼17.6 arcsec for the 250 μm band) but separated by distances greater than the SMA beamsize (∼2 arcsec) and lying below their detection threshold, with simple flux calculations indicating that these multiple systems should contain ≥3 individual DSFGs. Based on this assumption, G20 estimated that ∼60 per cent of faint ($S_{500} <$ 60 mJy) 500 μm risers and ∼35 per cent of bright ($S_{500} > 60$ mJy) 500 μm risers should be blends, indicating that this population is likely much more diverse than predicted. Similarly, based on LMT/AzTEC 1.1 mm follow-up observations of their sample of bright *Herschel* 500 μm risers, Montaña et al. (2021) find that 45/93 have no counterpart in the higher resolution imaging, with some of these non-detections expected to be multiple systems and others expected to be individual, resolved sources that are faint at 1.1 mm due to a large dust spectral emissivity index β. The multiplicity of their sample could therefore be ∼9 per cent in the most conservative scenario, or ∼50–60 per cent in the most extreme scenario. Any systems with high multiplicities would naturally be candidate high-redshift protocluster cores containing numerous DSFGs, structures discovered in only a handful of studies to date (e.g. Miller et al. 2018; Oteo et al. 2018).

A more robust estimate of the multiplicity fraction of 500 μm risers requires deeper, high-resolution follow-up observations. We followed on from G20 and targeted four of their 500 μm risers without an apparent SMA counterpart for additional, deeper FIR/sub-mm observations. Given the significant improvements to the SMA since 2015 (particularly in terms of the improved bandwidth provided by the SWARM correlator), we were able to obtain much deeper, high-resolution SMA 345 GHz continuum imaging of these 500 μm risers. We additionally obtained complementary observations at 850 μm with the Submillimeter Common User Bolometer Array 2 (SCUBA-2: Holland et al. 2013) on JCMT, providing an integrated flux density with a coarser resolution at a similar wavelength. The primary aim of this paper is to determine the multiplicities of these sources, allowing us to comment further on the diversity of the 500 μm riser population. The SCUBA-2 observations also allow us to investigate the wider field surrounding these sources and hence evaluate the environments in which they reside.

This paper is structured as follows: In Section 2, we describe the selection of the 500 μm riser sample, followed by a discussion of the observations and data reduction in Section 3. In Sections 4 and 5, we present the results of this study and discuss the properties of our 500 μm risers, followed by the conclusions and summary in Section 6. Throughout this work, we adopt the standard flat Λ cold dark matter cosmology: $\Omega_{\mathrm{m}} = 0.3$, $\Omega_{\Lambda} = 0.7$, and $H_0 = 70\,\mathrm{km\,s^{-1}\,Mpc^{-1}}$.

2 SAMPLE SELECTION

A full description of the selection of the original sample of 500 μm risers is provided in G20. Here, we briefly outline the main points of this selection. G20 select a heterogeneous sample of 34 500-μm risers based only on their *Herschel* SPIRE flux densities and colours ($S_{250} < S_{350} < S_{500}$) from HerMES. The sample has an average 500 μm flux density of 67 ± 29 mJy and all sources are detected to $>4\sigma$. G20 note that recent refinements to the data reduction process means that the flux densities of sources in the sample vary in the most recent maps and catalogues, such that ∼7/34 cannot now be strictly defined as 500 μm risers. These sources are still included, as flux boosting is known to introduce some variation into the *Herschel* colours of 500 μm risers, and typical star-forming SED shapes indicate that these sources could still lie at high redshift. G20 used the ALESS

Downloaded from academic.oup.com/mnras/article/519/1/709/6849985 by Imperial College of Science Technology and Medicine user on 19 October 2026

Table 1. Positions and integrated FIR/sub-mm photometry for the four 500 μm risers. *Herschel* SPIRE flux densities are taken from G20. The integrated 870 μm flux density is calculated by summing the SMA flux densities (corrected for primary beam response) of all sources associated with each 500 μm riser in Table 2.

Source	RA [J2000]	Dec. [J2000]	$S_{250\mu m}$ [mJy]	$S_{350\mu m}$ [mJy]	$S_{500\mu m}$ [mJy]	$S_{850\mu m}$ [mJy]	$S_{870\mu m}$ [mJy]	$S_{1.4mm}$ [mJy]
Bootes15	14:40:09.66	+34:37:55.70	51.2 ± 6.0	68.3 ± 7.0	66.1 ± 8.0	2.6 ± 1.5	3.2 ± 0.4	–
Bootes24	14:36:21.30	+33:02:29.00	28.7 ± 6.0	49.7 ± 7.0	55.8 ± 8.0	11.3 ± 2.6	6.8 ± 0.6	–
Bootes27	14:38:45.14	+33:22:31.80	37.8 ± 6.0	44.2 ± 7.0	52.2 ± 8.0	10.1 ± 1.6	1.9 ± 0.4	–
XMM-M5	02:18:56.74	−04:35:44.90	26.6 ± 6.0	44.0 ± 7.0	46.1 ± 8.0	8.1 ± 3.3	–	1.3 ± 0.3

(da Cunha et al. 2015) average SED at $z = 4$–6 and normalized to a 500 μm flux density of 60 mJy to estimate that, given their observed sub-mm flux densities and assuming that a single source is responsible for the total *Herschel* flux density, these sources should have flux densities of ∼24–38 mJy at 345 GHz. However, despite reaching detection thresholds of ∼7–10 mJy, 12 maps showed no detections. Assuming in the most conservative case that any multiple systems are comprised of sources with similar flux densities, G20 predicted that these 500 μm risers must break up into ≥3 sources, and are therefore potential indications of forming compact cluster cores at $z > 4$ similar to those discovered by Oteo et al. (2018) and Miller et al. (2018).

We selected the three brightest sources at 500 μm from the 12 sources in the G20 sample without SMA counterparts (Bootes15, Bootes24, and Bootes27) for multiwavelength follow-up observations. Another 500 μm riser that remained undetected in the follow-up observations of G20 (XMM-M5) is also considered in this analysis. XMM-M5 is somewhat fainter at 500 μm than the three Bootes sources but, given the 9.1 mJy detection limit in the SMA observations of G20, should still have been comfortably detected in these observations. The SMA observations of XMM-M5 presented in this paper were taken as part of a separate SMA project, and were tuned to a different frequency than the three sources in the Bootes field. These observations will be discussed further in Section 3.

The positions and *Herschel* SPIRE photometry for our four target sources are presented in Table 1, and in Fig. 1 we show their *Herschel* SPIRE colours. We find that our 500 μm risers are quite typical of the majority of the global 500 μm riser population, although potentially lying towards the less extreme end.

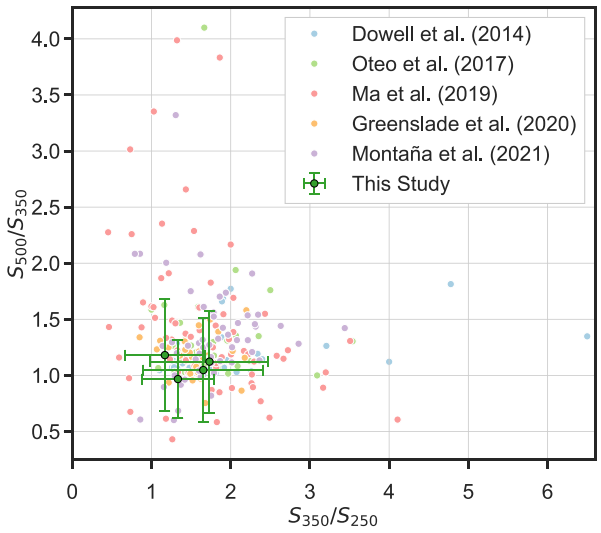


Figure 1. *Herschel* SPIRE colours for our 500 μm risers alongside those from a selection of studies in the literature. Note that the Ma et al. (2019) and Montaña et al. (2021) colours are based on deblended *Herschel* photometry using high-resolution follow-up observations and so contain a number of sources that are no longer strictly 500 μm risers. We find that our 500 μm risers are towards the less extreme end of the global 500 μm riser population.

3 OBSERVATIONS AND DATA REDUCTION

3.1 SMA observations

The SMA observations were taken in three tracks between 2020 January 31 and 2020 February 26 as part of the SMA program 2019B-S016 (PI: J. Cairns), with total integration times of 10.9 h on Bootes15, 4.6 h on Bootes24, and 3.6 h on Bootes27. These integration times are an improvement over the follow-up observations of G20, who targeted these sources for 3.9, 3.7, and 2.2 h, and they compare favourably to the average integration time of 4.1 h across all G20 follow-up observations. The conditions for these observations were exquisite, with τ values of ∼0.02–0.04. We used the SMA in its COM configuration with seven antennae, resulting in a beamsize of ∼1.7 arcsec × 2.1 arcsec. The SMA uses two receivers, each with two sidebands of 8 GHz separated by a gap of 8 GHz, and with each sideband separated into four chunks. We tuned these two receivers to 337 and 345 GHz, respectively, to produce 32 GHz of continuous bandwidth for our observations.

We reduced our SMA maps using the standard IDL-based SMA data reduction package MIR.[1] First, we manually inspected the data, flagging any regions that contained phase jumps and fixing any channels that contained significant noise spikes, before applying the system temperature correction. The passband calibration was completed using the sources 3c454.3, 3c279, 0927+390, or 3c84, while for flux calibration, we used either 0854+201 or Callisto. Gain calibration on the SMA is carried out by periodically observing nearby bright quasars with known flux densities alternately to the desired source. For these purposes, we used the quasars 1506+426 and 3c345. The error for this calibration process is estimated to be ∼10 per cent (see e.g. Liu et al. 2018).

We then used the Common Astronomy Software Applications package[2] (CASA: McMullin et al. 2007) to complete the imaging. Following the calibration process in MIR, each chunk of each sideband on each receiver is exported into CASA, before being concatenated together to produce one large visibility data set. We manually flagged the ∼300 channels on the edge of each chunk in order to avoid including poor data in the final image, inspecting the result to ensure that we had flagged enough of the edge channels and that there were

[1] https://github.com/qi-molecules/sma-mir
[2] https://casa.nrao.edu/index.shtml

Downloaded from academic.oup.com/mnras/article/519/1/709/6849985 by Imperial College of Science Technology and Medicine user on 19 October 2026

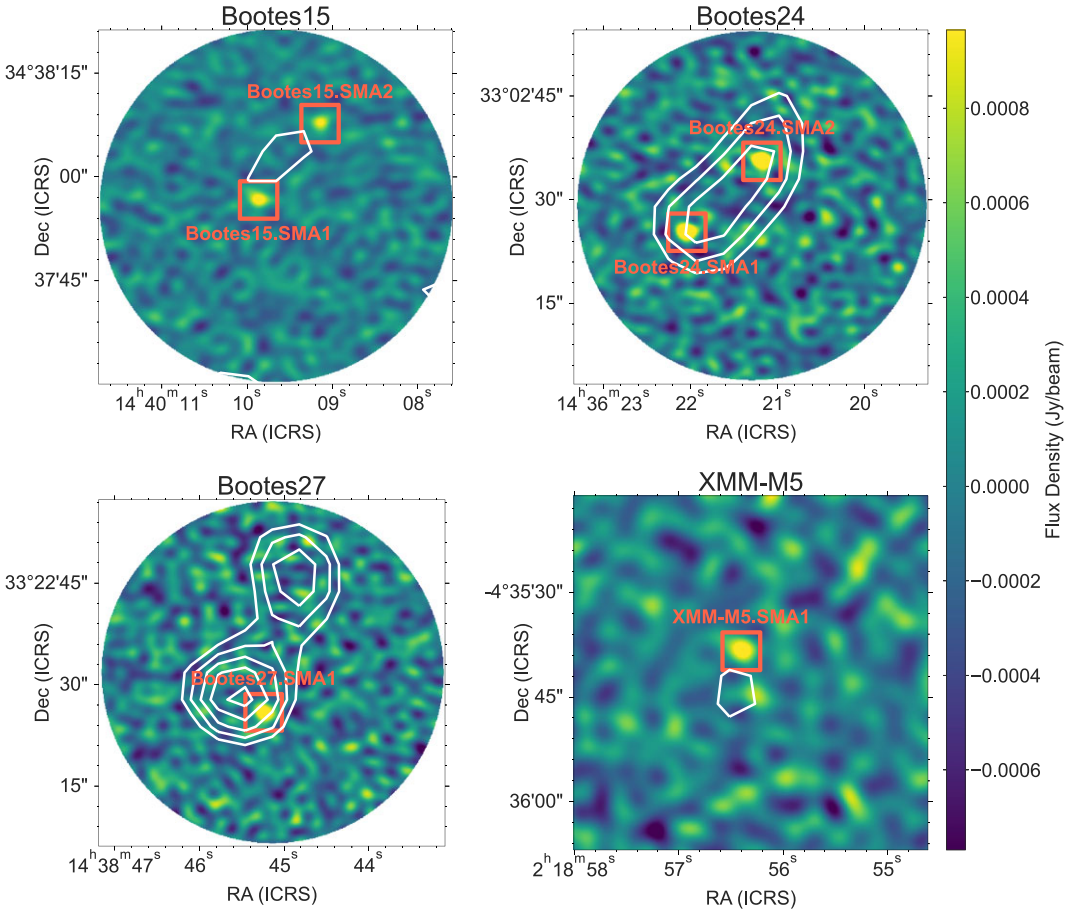


Figure 2. SMA maps overlaid with SCUBA-2 850 μm contours from 3σ to 7σ significance for the four 500 μm risers. Bootes15 and Bootes24 each break up into two individual sources in the SMA maps, while Bootes27 and XMM-M5 each resolve into one faint source. Bootes24 and Bootes27 are well detected by SCUBA-2, with Bootes27 in particular showing two partially resolved sources, while Bootes15 and XMM-M5 are marginally detected to ∼3σ significance.

no spikes or strong lines in the data. We generated the continuum by averaging all of the remaining spectral channels together.

In order to clean the SMA maps, we identified the positions of likely sources from the dirty maps. The first step of this process was to estimate a detection threshold for each of our SMA maps following the method of G20. For each map we generated 1000 fake noise maps with the same dimensions containing Gaussian random noise. Each of these maps was then convolved with the SMA beam for that observation and scaled to match the noise characteristics of the real SMA map. We extracted sources from each of these fake noise maps based on a range of signal-to-noise thresholds from 2 to 5 in steps of 0.05, considering as detections any source with a peak pixel value greater than the given signal-to-noise threshold, and any other surrounding pixels within the SMA beamsize meeting the signal-to-noise criteria considered part of the same source. For each signal-to-noise threshold value, we averaged the number of fake sources extracted across the 1000 realizations. The optimal signal-to-noise threshold will be low enough to allow us to extract sources deep into the SMA maps, but high enough to minimize the number of fake sources extracted from the fake noise maps. Following G20, we selected a signal-to-noise cut-off corresponding to an average of 0.1 extracted fake sources across all 1000 realizations, yielding a detection threshold of 4.1σ for the three maps in the Bootes field, slightly higher than the average value of 3.75σ found for the G20 observations.

We found all sources above this 4.1σ detection threshold in the dirty maps and considered them to be real. We used the CASA command `tclean` to complete interactive CLEANing of our SMA maps. We selected natural weighting which maximizes the signal-to-noise and used <100 CLEAN iterations for each map, placing CLEAN windows in the images to select flux only from the positions of the >4.1σ detections. The resulting CLEANed maps reached 1σ RMS values of 0.17, 0.29, and 0.27 mJy beam^{-1} for Bootes15, Bootes24, and Bootes27, respectively, around an order-of-magnitude deeper than the maps obtained by G20.

XMM-M5 was observed as part of the SMA project 2019A-S004 (PI: D. L. Clements). The observations and subsequent data reduction will be discussed in a forthcoming paper (Clements et al. in preparation) and we simply highlight the important features here. The SMA was used in its COM configuration with the two receivers tuned to 198 and 206 GHz, respectively, resulting in a beamsize of ∼3.6 arcsec × 3.2 arcsec. We estimate the optimum detection threshold for the XMM-M5 map using the above method, finding a slightly higher value of 4.3σ. The reduced SMA map for XMM-M5 has a 1σ RMS sensitivity of ∼0.28 mJy beam^{-1}. The CLEANed SMA maps for all four sources are shown in Fig. 2.

We tested the completeness of our SMA maps by inserting fake sources matching the beamshape of the SMA observations at random positions within the dirty maps, observing how many of the fake sources were recovered. The details of these calculations

Downloaded from academic.oup.com/mnras/article/519/1/709/6849985 by Imperial College of Science Technology and Medicine user on 19 October 2026

are discussed in Appendix A. We find that Bootes15 performs significantly better than the other maps, reaching 100 per cent completeness for sources with flux densities $\geq$1.1 mJy. Bootes24 and Bootes27 reach a completeness of 50 per cent at 1.6 and 1.2 mJy, 80 per cent at 1.9 and 1.4 mJy, and up to 100 per cent at 2 and 1.7 mJy, respectively. XMM-M5 reaches 50 per cent completeness at 1.3 mJy, but does not reach 100 per cent completeness until 2.1 mJy.

3.2 SCUBA-2 observations

3.2.1 Reduction and calibration

The SCUBA-2 450 and 850 μm observations for Bootes15, Bootes24, and Bootes27 were taken between 2020 December 1 and 2021 January 20 as part of the SCUBA-2 program M20BP036 (PI: J. Cairns). Each source was observed with several pointings using the CV Daisy mode, with a total of ∼2.7 h on Bootes15, ∼1.4 h on Bootes24, and ∼4.1 h on Bootes27. Weather conditions were typically between Band 2 and Band 3, with τ_{225} values in the range 0.08–0.14, allowing us to reach 1σ RMS sensitivities of 2.2, 2.8, and 1.7 mJy beam^{-1} in our SCUBA-2 850 μm maps of Bootes15, Bootes24, and Bootes27, respectively. We reduced our observations using the Sub-Millimetre User Reduction Facility (SMURF) package (Chapin et al. 2013) and the ORAC-DR data reduction pipeline (Economou et al. 1999).

For our first data reduction method, we used the ORAC-DR data reduction pipeline with the REDUCE_SCAN_FAINT_POINT_SOURCES recipe. Raw data are passed to the map maker to produce an image calibrated in mJy beam^{-1}. The pipeline then estimates the RMS noise in the image and calculates the Noise Equivalent Flux Density (NEFD). Once all the individual observations have been processed, the pipeline co-adds individual scans together, which it then convolves with a matched filter to enhance the signal-to-noise ratio (SNR) of point sources. The RMS noise and NEFD are calculated for this co-added image, and a signal-to-noise map is produced. We additionally completed a second data reduction using the ORAC-DR pipeline with the REDUCE_SCAN_EXTENDED_SOURCES recipe. Given that the SCUBA-2 beamsize is smaller than that of *Herschel* SPIRE at 250 μm but larger than that of the SMA, it is possible that any multiple systems may be partially resolved in the SCUBA-2 850 μm maps. In this case, flux density estimates should be calculated based on SCUBA-2 maps reduced without the matched filter to avoid missing flux for the partially resolved sources lying outside of the SCUBA-2 beam. The REDUCE_SCAN_EXTENDED_SOURCES recipe passes the raw data for the individual scans to the map maker which processes them to produce a Frame image, which is then calibrated in units of mJy arcsec^{-2}. Individual scans are co-added together and the noise properties of the image are calculated. While the SCUBA-2 instrument simultaneously provides 450 and 850 μm photometry, the noise levels in the 450 μm maps were too large to detect our 500 μm risers based on their *Herschel* SPIRE flux densities.

We used archival 850 μm SCUBA-2 maps for XMM-M5 from the Canadian Astronomy Data Center. XMM-M5 was observed as part of the SCUBA-2 Large eXtragalactic Survey (S2LXS[3]: Geach et al. M17BL001) and is present in two overlapping pointings. We re-reduced each of these pointings using the ORAC-DR pipeline as outlined above, and co-added the two pointings to obtain a deeper SCUBA-2 850 μm image of XMM-M5. After this reduction process, we find that the RMS noise in an aperture of radius 350 arcsec centred on the SMA position of XMM-M5 is ∼3.3 mJy beam^{-1}. In Fig. 2, we show the SMA maps for the 500 μm risers with 850 μm contours based on the REDUCE_SCAN_FAINT_POINT_SOURCES reduced SCUBA-2 maps. The SCUBA-2 maps with the matched filter were chosen for Fig. 2 as this reduction maximizes the SNR in the map.

3.2.2 False detection rates and completeness

We test the reliability in our SCUBA-2 maps using two separate methods. For the first method, we invert our SCUBA-2 point source reduced maps and find any >4σ negative noise peaks. Assuming that there are roughly equal numbers of positive and negative spurious peaks in our SCUBA-2 maps, taking the ratio of these negative peaks to the total number of positive >4σ peaks should give us a reasonable estimate of how many of our sources are spurious. For the Bootes15 and XMM-M5 fields, the reliability is $\gtrsim$ 80 per cent at 4σ, similar to other analyses of this nature (MacKenzie et al. 2017; Cheng et al. 2019). For the Bootes24 and Bootes27 fields, the reliability drops to ∼60 per cent and ∼50 per cent, respectively. The second method uses 'jackknife' maps to estimate the reliability. First, we used the MAKEMAP command in the SMURF package to create an individual map for each of the available SCUBA-2 scans. We then invert half of these maps before co-adding all scans together to produce a single map with the sources removed (i.e. containing just noise). As with the previous reductions, we then applied a matched filter and subsequently produced a signal-to-noise map for each field. We find that the Bootes15 and Bootes24 fields both have a 100 per cent reliability at 4σ based on the jackknife maps, while the Bootes27 field has a reliability of ∼88 per cent. XMM-M5 has a somewhat lower reliability of 60 per cent using this method. The reliability estimates based on the jackknife maps are likely more robust as they do not rely on the assumption that there are the same number of spurious positive and negative noise spikes in the maps. We additionally tested the reliability for numerous different reductions in which we co-added various combinations of the available SCUBA-2 integrations for each field. The aforementioned reliability values, and the following discussions, are based on those combinations of integrations with the highest reliabilities.

To test the completeness of our SCUBA-2 point source maps, we inserted fake sources at random positions within the SCUBA-2 map and observed how many of the fake sources were recovered to >4σ. The details of this completeness calculation are discussed in Appendix A. We find that Bootes15 and Bootes27 both reach a completeness of ∼50 per cent at ∼10 mJy, and rise to a completeness of $\gtrsim$ 80 per cent at 14 mJy. By comparison, Bootes24 and XMM-M5 have a slightly poorer completeness, reaching ∼80 per cent at ∼17 mJy and ∼16 mJy, respectively.

3.3 Extracting flux densities

We then extracted flux densities from the SMA and SCUBA-2 maps. Following G20, we simply extracted peak flux densities from the CLEANed SMA maps for each source detected to >4.1σ in the dirty SMA maps. These flux densities were then corrected for the primary beam response which, for the SMA, can be described as a Gaussian function with a size determined by the wavelength of the observations.[4] We used the pbplot command in the MIRIAD

[3]https://www.eaobservatory.org/jcmt/science/large-programs/s2lxs/

[4]https://lweb.cfa.harvard.edu/sma/miriad/manuals/SMAuguide/smauserhtml/node130.html

Downloaded from academic.oup.com/mnras/article/519/1/709/6849985 by Imperial College of Science Technology and Medicine user on 19 October 2026

Table 2. Positions, corrected SMA flux densities, and primary beam response values for the resolved SMA sources associated with each 500 μm riser.

Source	RA [J2000]	Dec. [J2000]	$S_{870\mu m}$ [mJy]	Primary beam Response
Bootes15.SMA1	14:40:09.86	+34:37:56.65	1.4 ± 0.2	0.98
Bootes15.SMA2	14:40:09.13	+34:38:07.84	1.8 ± 0.3	0.60
Bootes24.SMA1	14:36:22.04	+33:02:25.30	3.4 ± 0.5	0.76
Bootes24.SMA2	14:36:21.17	+33:02:35.53	3.4 ± 0.5	0.88
Bootes27.SMA1	14:38:45.24	+33:22:25.92	1.9 ± 0.4	0.91
XMM-M5.SMA1	02:18:56.39	−04:35:38.32	1.3 ± 0.3†	0.99

Note. †SMA observations tuned to 210 GHz rather than 345 GHz.

(Sault, Teuben & Wright 2011) package to determine the full width at half-maximum (FWHM) of the SMA primary beam at 345 GHz for our three sources in the Bootes field, and at 210 GHz for XMM-M5. We then found the primary beam response at the position of the peak flux density value for each source, and divided the extracted flux density by this value, propagating the errors accordingly. In Table 2, we present the corrected SMA photometry alongside the corresponding correction factor for the primary beam response, where the uncertainties include the 10 per cent calibration error added in quadrature with the RMS noise in the SMA map. We also extracted flux densities from the dirty SMA maps using a similar method, finding that they differ by no more than ∼3 per cent from those extracted from the CLEANed maps.

For the SCUBA-2 850 μm maps, we extracted two separate flux densities for our 500 μm risers, one for each of the two pipeline reductions. For the 850 μm map reduced using the `REDUCE_SCAN_FAINT_POINT_SOURCES` recipe, we simply locate the highest signal-to-noise pixel associated with the 500 μm riser. For the 850 μm map reduced using the `REDUCE_SCAN_EXTENDED_SOURCES` recipe, we laid down a series of apertures in the image with increasing radii from 0 to 10 arcsec at the position of the brightest pixel in the *Herschel* SPIRE 250 μm image. We additionally tested placing these apertures at the position of the brightest pixel associated with each 500 μm riser in the SCUBA-2 850 μm point source maps, finding that the extracted flux density is exceedingly similar. This produces a flux density in units of mJy arcsec^{-2}, which we then multiplied by 16 in order to convert to mJy (based on the 4 arcsec pixel size of the SCUBA-2 850 μm images). For the final flux density measurement, we selected the aperture with the largest flux density value, as this aperture should contain the maximum amount of flux density from the source without including too much contaminating background (we also manually checked each final aperture to make sure that it was a reasonable size).

SCUBA-2 850 μm photometry must be corrected for flux boosting. Geach et al. (2017) investigated the effects of flux boosting in the SCUBA-2 Cosmology Legacy Survey (S2CLS), finding that the level of flux boosting is consistent across the whole survey and well described by the power law

$$B = 1 + 0.2\left(\frac{\mathrm{SNR}}{5}\right)^{-2.3}, \quad (1)$$

where B is the flux boosting factor and SNR is the SNR of the detection. We estimated errors for our SCUBA-2 flux densities based on the combination of instrumental noise, confusion noise, a typically assumed 5 per cent calibration error, and the uncertainty in the flux boosting, which we define as the difference between the extracted and deboosted flux densities. The SCUBA-2 850 μm flux densities can be found in Table 3.

We then investigated the environments surrounding our four 500 μm risers using the point source reduced maps (as this reduction yields the highest signal-to-noise). We first cropped the SCUBA-2 maps to a circle of diameter 700 arcsec centred on the position of the SCUBA-2 detection, removing the edges of the map where the variance becomes much larger. For each SNR map, we found all pixels with SNR > 4, with connected pixels considered part of the same source. We then manually examined the extracted sources to ensure that only SNR > 4 detections are included and that there is no evidence of shredding. In Appendix B, we present the reduced SCUBA-2 850 μm maps and positions of the detected sources. For each source, we estimated deboosted flux densities and errors following the method outlined above, which are presented in Table 4.

4 RESULTS

4.1 SMA and SCUBA-2 detections

In Fig. 2, we present the SMA maps for the four 500 μm risers, overlaid with SCUBA-2 850 μm contours. In Fig. 3, we present a similar plot showing the 250 μm *Herschel* SPIRE map overlaid with both SCUBA-2 850 μm and SMA contours. We find that Bootes15 and Bootes24 each break up into two bright sources, both of which are detected to $>5\sigma$ in both the dirty and CLEANed SMA maps. Bootes27 resolves into a single bright source detected to $>5\sigma$, but we note that there are other marginally detected sources in the map. In particular, we find a second source detected to $\sim3.9\sigma$ in the dirty map and $\sim3.1\sigma$ in the CLEANed map, offset by ∼10 arcsec from the edge of the observed SCUBA-2 3σ emission region. This source has a flux density of ∼1.2 mJy in the dirty map, uncorrected for the primary beam response. At this flux density level, the Bootes27 SMA dirty map has a completeness of ≈ 60 per cent, and so we would not necessarily expect to observe this source above our nominal signal-to-noise threshold. There is another marginal $\sim3.3\sigma$ detection in the dirty SMA map coinciding with the Northern component of the SCUBA-2 contours (Fig. 3) with a flux density of ∼1.0 mJy in the dirty map. At this flux density level, the SMA map for Bootes27 has a completeness of just 20 per cent, so it is not surprising that this source remains undetected. However, we extract a primary-beam-corrected flux density from the CLEANed map of 2.9 ± 0.9 mJy for this source, indicating that it could provide a significant contribution to the integrated sub-mm flux density. However, these detections fall below our nominal 4.1σ detection threshold, and so we do not consider them to be robust. As such they are not included in the forthcoming analysis, although their potential significance is

Downloaded from academic.oup.com/mnras/article/519/1/709/6849985 by Imperial College of Science Technology and Medicine user on 19 October 2026

Table 3. SCUBA-2 850 μm flux densities for our four targets. The point source flux density is derived from the map reduced with the REDUCE_SCAN_FAINT_POINT_SOURCES recipe. The extended flux density is derived from the map reduced using the REDUCE_SCAN_EXTENDED_SOURCES recipe, and in this case we also provide the aperture radius used for the flux density estimate. For Bootes27, we report separate flux density estimates for the two partially resolved detections in the point source reduced maps.

Source	Point source flux density [mJy]	Extended flux density [mJy]	Extended aperture radius [arcsec]
Bootes15	2.9 ± 1.8	2.6 ± 1.5	14.0
Bootes24	9.7 ± 2.2	11.3 ± 2.6	19.2
Bootes27	–	10.1 ± 1.6	20.0
Bootes27.1†	6.9 ± 1.3	–	–
Bootes27.2†	5.6 ± 1.3	–	–
XMM-M5	8.1 ± 3.3	–	–

Note. †Partially resolved components

Table 4. Positions and integrated FIR/sub-mm photometry for the SNR > 4 SCUBA-2 detections with HerMES counterparts. *Herschel* SPIRE flux densities are taken from the corresponding HerMES catalogue.

Source	RA [J2000]	Dec. [J2000]	$S_{250\mu m}$ [mJy]	$S_{350\mu m}$ [mJy]	$S_{500\mu m}$ [mJy]	$S_{850\mu m}$ [mJy]
Bootes15.SCUBA1	14:39:46.10	+34:35:18.74	0.0 ± 3.5	15.0 ± 2.3	13.4 ± 2.7	11.7 ± 3.1
Bootes15.SCUBA2	14:40:17.23	+34:36:45.19	6.8 ± 2.8	24.1 ± 3.0	0.0 ± 4.4	6.0 ± 1.7
Bootes15.SCUBA3	14:39:54.99	+34:39:24.67	25.0 ± 2.3	40.1 ± 2.3	32.9 ± 3.0	9.1 ± 2.1
Bootes24.SCUBA1	14:36:27.67	+33:03:05.02	46.1 ± 2.2	48.2 ± 2.6	28.7 ± 4.1	15.3 ± 2.5
Bootes24.SCUBA2	14:36:20.49	+33:06:29.46	73.7 ± 2.3	79.5 ± 2.4	57.0 ± 3.2	18.7 ± 4.8
Bootes27.SCUBA1	14:38:51.21	+33:20:55.74	19.6 ± 2.3	26.8 ± 2.3	29.0 ± 2.7	5.7 ± 1.4
Bootes27.SCUBA2	14:38:37.17	+33:23:12.26	47.9 ± 2.3	25.4 ± 2.3	26.5 ± 3.2	6.5 ± 1.6
Bootes27.SCUBA3	14:38:39.71	+33:23:27.66	564.2 ± 4.6	219.7 ± 10.2	83.8 ± 17.8	11.3 ± 1.6
XMM-M5.SCUBA1	02:19:14.18	−04:37:38.09	25.7 ± 1.0	37.7 ± 1.1	37.9 ± 1.4	10.5 ± 3.5
XMM-M5.SCUBA2	02:18:35.31	−04:36:02.25	15.4 ± 1.1	14.6 ± 1.0	7.7 ± 1.3	13.7 ± 3.9
XMM-M5.SCUBA3	02:18:57.87	−04:33:51.44	81.5 ± 1.1	70.7 ± 1.2	40.9 ± 1.9	10.0 ± 3.4

discussed. The SMA map for XMM-M5 shows a single ∼4.7σ peak coincident with the bright *Herschel* 500 μm riser (Fig. 3).

The SCUBA-2 850 μm contours in Figs 2 and 3 demonstrate that XMM-M5 is marginally detected as a point-like source with an SNR of 3.65. Bootes15 is also marginally detected with an SNR of 3.06, but is likely to be extended as the SCUBA-2 flux density peaks between the two SMA detections and is elongated along the direction of their separation. By comparison, Bootes24 and Bootes27 are both well detected to >5σ and appear partially resolved in the SCUBA-2 contours. Bootes27 in particular is clearly comprised of two partially resolved sources, a Southern component coincident with the single resolved SMA source, and a Northern component with no apparent SMA cross-match, except for the 3.3σ marginal detection. In Table 3, we present the flux density estimates for the four targets based on both the point source and extended source SCUBA-2 reductions. We additionally show the aperture radius used for estimating the flux density for the extended reduction. For Bootes27, we present two separate flux density estimates for each of the partially resolved components in the point source reduced maps. Finally, we note that no reliable flux density could be extracted for XMM-M5 in the extended source maps. These estimates are present in Table 3.

The flux density estimates from the two pipeline reduction methods broadly agree within the errors. For the analysis in this paper, we will use the flux density from the REDUCE_SCAN_FAINT_POINT_SOURCES reduction for XMM-M5 which appears as a point source in the SCUBA-2 maps, and the flux densities from the REDUCE_SCAN_EXTENDED_SOURCES reduction for Bootes15 and Bootes24, which appear as extended sources. When considering the total Bootes27 system, we will use the flux density from the extended source maps, but the two partially resolved components in the point source maps will be discussed in more detail as well. We additionally note that, while Bootes15 and XMM-M5 are detected to >3σ in the SCUBA-2 850 μm maps, after including the instrumental, confusion, and calibration uncertainties, the photometry is constrained to an accuracy of ∼1.7σ and ∼2.5σ, respectively.

In Table 1, we present the integrated FIR/sub-mm photometry for the four 500 μm risers, where we have estimated the total SMA flux density for each source by adding together the flux densities of the resolved sources in the SMA continuum maps from Table 2. We find that, despite being observed at similar wavelengths, we measure integrated flux densities for Bootes27 of 10.1 ± 1.6 mJy and 1.9 ± 0.3 mJy from the SCUBA-2 and SMA maps, respectively, indicating a >4σ disparity between the two measurements. We investigate this discrepancy by plotting the SCUBA-2 850 μm flux density against the SMA continuum flux density at ∼870 μm for each of the 500 μm risers alongside similar studies which obtained both interferometric and single-dish sub-mm photometry. Hill et al. (2018) targeted 70 of the brightest 850 μm sources from S2CLS down to a limiting flux density of S_{850} ∼ 8 mJy with high-resolution SMA follow-up observations at 860 μm. Similarly, Stach et al. (2019) present the ALMA survey of the SCUBA-2 Cosmology Legacy Survey UKIDSS/UDS field (AS2UDS), providing high-resolution,

Downloaded from academic.oup.com/mnras/article/519/1/709/6849985 by Imperial College of Science Technology and Medicine user on 19 October 2026

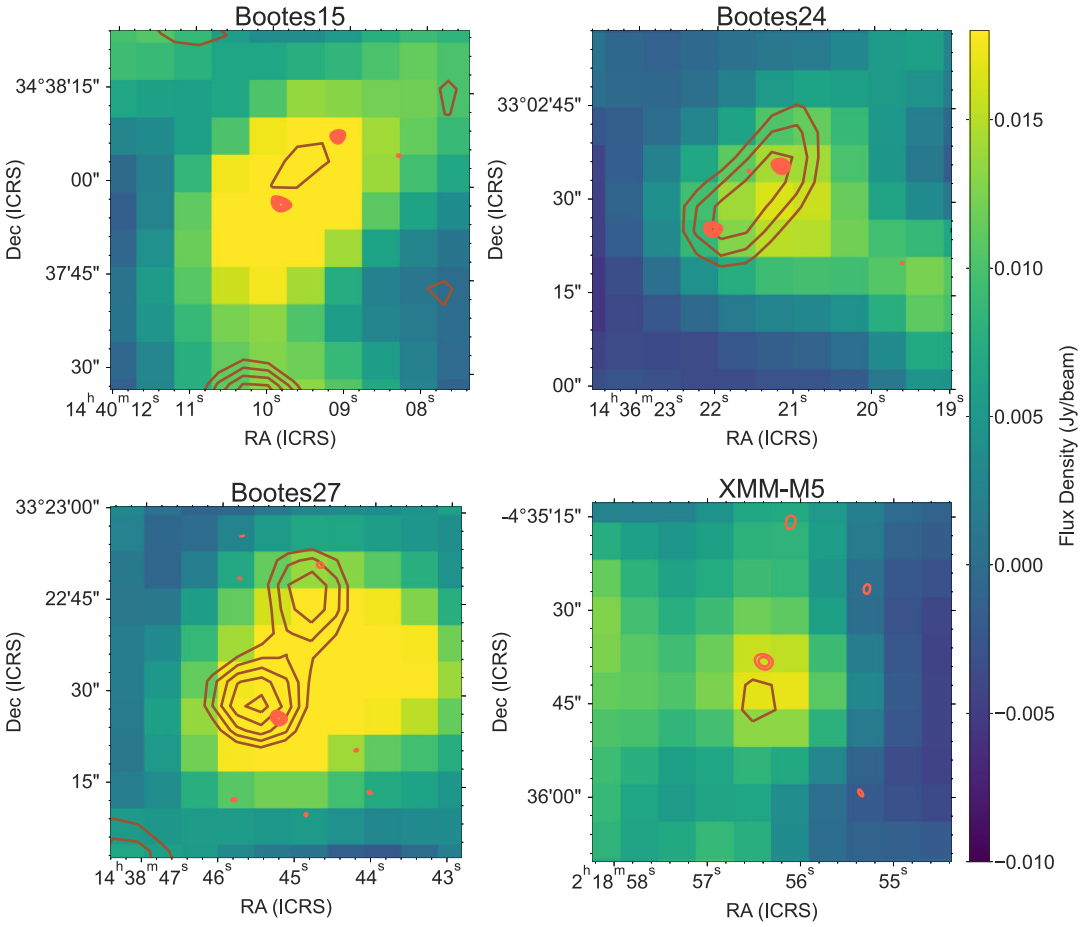


Figure 3. *Herschel* SPIRE 250 μm maps with SCUBA-2 850 μm (brown) and SMA (red) contours from 3σ to 7σ significance for the four 500 μm risers. Bootes15, Bootes24, and Bootes27 each break up into two individual sources in the SMA maps, while XMM-M5 resolves into one faint source. Bootes24 and Bootes27 are well detected by SCUBA-2, while Bootes15 and XMM-M5 are marginally detected to ∼3σ significance. Bootes27 shows two partially resolved SCUBA-2 sources associated with the bright *Herschel* source.

ALMA Band 7 follow-up observations of SCUBA-2 850 μm sources in the UKIDSS/UDS field. We combined the SMA, ALMA, and SCUBA-2 photometry from these surveys and, for any SCUBA-2 sources which break up into multiple components in the higher resolution interferometric observations, we add the flux densities of the resolved sources together in order to compare with our own photometry. The result of this comparison is shown in Fig. 4. We find that the SMA and SCUBA-2 flux densities are consistent for Bootes15, and are within 3σ of each other for Bootes24. For Bootes27, the single resolved SMA source coincident with the SCUBA-2 contours is approximately five times fainter than the integrated flux density from the SCUBA-2 maps, placing it well outside of the region probed by the Hill et al. (2018) and Stach et al. (2019) samples. We interpret this disparity as evidence of additional faint sources lying below the SMA detection limit, but contributing to the integrated flux density at 850 μm. We note that, should the marginal detection associated with the Northern component of the SCUBA-2 contours be considered, this disparity is reduced, with the integrated sub-mm flux density being just over twice as bright as the summed SMA flux densities in this case.

Moreover, we find that the integrated SCUBA-2 850 μm flux densities of our 500 μm risers are somewhat lower than we might expect based on their *Herschel* SPIRE colours. In Fig. 5, we compare the integrated 500 and 850 μm flux densities of our 500 μm risers, alongside the S2CLS and STUDIES (SCUBA-2 Ultra Deep Imaging EAO Survey: Wang et al. 2017) samples. While the FIR/sub-mm photometry for Bootes24, Bootes27, and XMM-M5 is reasonably consistent with the brighter end of S2CLS and STUDIES, Bootes15 is significantly fainter at 850 μm than sources with similar 500 μm flux densities. We investigate the possibility that there are additional sources blended within the 500 μm *Herschel* SPIRE beam that do not contribute to the SCUBA-2 flux density. Comparing the three *Herschel* SPIRE images and the SCUBA-2 map for Bootes15, we find that one of the SNR > 4 SCUBA-2 detections lies ≈31 arcsec to the South of Bootes15, placing it just within the FWHM of the *Herschel* SPIRE beamsize at 500 μm (35.2 arcsec) but outside of the 250 μm (17.6 arcsec) and 350 μm (23.9 arcsec) beamsize. This SCUBA-2 source does not have a separate counterpart in the HerMES catalogues, indicating that it would not have been deblended from the Bootes15 detection, and so may contribute to making Bootes15 artificially red. Similarly, we find a SCUBA-2 detection towards the South East of Bootes27 within the 500 μm beamsize which may contribute to making this source artificially red. For Bootes24 and XMM-M5, all SNR > 4 SCUBA-2 detections lie well outside of the *Herschel* SPIRE 500 μm beamsize, and all nearby 250 μm sources are detected as separate objects in the HerMES catalogue. In Appendix C, we present a comparison of the *Herschel* SPIRE and SCUBA-2 images for our targets, as well as a discussion of the

Downloaded from academic.oup.com/mnras/article/519/1/709/6849985 by Imperial College of Science Technology and Medicine user on 19 October 2026

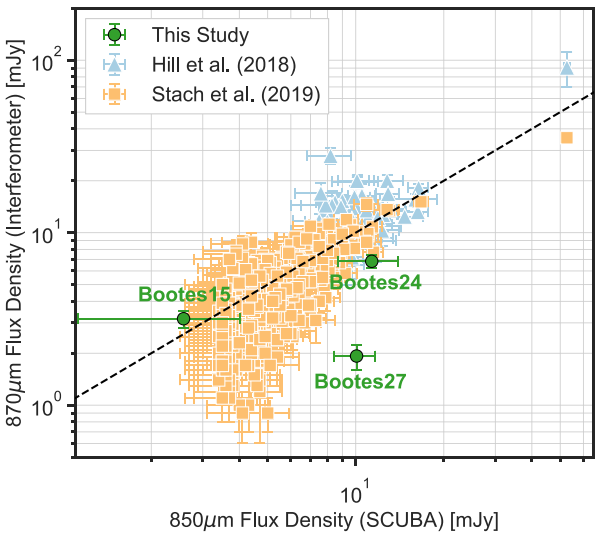


Figure 4. The combined 870 μm flux density for the resolved sources in either SMA or ALMA maps as a function of their integrated 850 μm flux density from SCUBA-2. The orange squares and blue triangles show the Stach et al. (2019) and Hill et al. (2018) samples, respectively, while the green points show our sample of 500 μm risers. The black dashed line shows where the two flux density measurements are equal. We do not include XMM-M5 in this plot as the SMA observations are tuned to a shorter wavelength (210 GHz rather than 345 GHz).

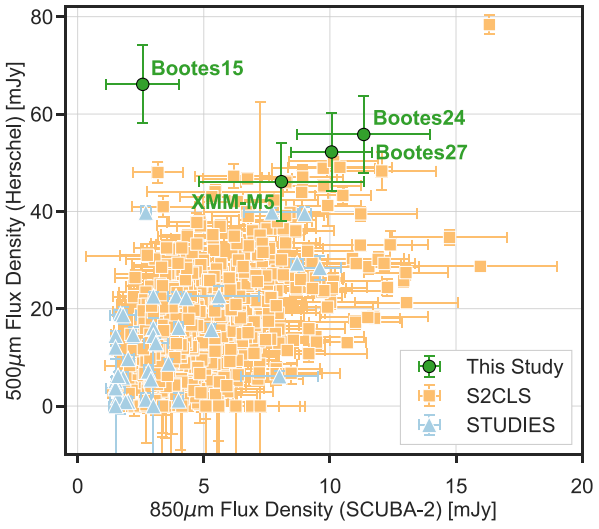


Figure 5. SCUBA-2 850 μm flux density versus *Herschel* SPIRE 500 μm flux density for our 500 μm risers (green points) as well as for the S2CLS (orange squares) and STUDIES (blue triangles) surveys. Bootes15 is significantly fainter than expected at 850 μm based on its 500 μm flux density.

likely effect of the contaminating sources associated with Bootes15 and Bootes27 on their flux densities at 350 and 500 μm, which we estimate to be small.

We additionally note, in Fig. 5, the possible presence of two diverging trends, a steeper gradient traced by our 500 μm risers, and a second, shallower trend at lower 500 μm flux densities. While based on small numbers of sources, this could suggest that the brighter end of the 850 μm population splits into two distinct populations with significantly different SED shapes in the FIR/sub-mm, potentially caused by different multiplicities, dust properties, or redshifts. Such a trend would require additional sources probing this rather sparse region, and follow-up observations to reveal the properties of DSFGs in these two distinct regions.

4.2 FIR/sub-mm colours

We have found that three quarters of our 500 μm risers suffer from blending. Bootes15 and Bootes24 break up into two distinct sources in the SMA observations, while Bootes27 is clearly comprised of two partially resolved sources in the SCUBA-2 observations. This source blending likely influences their FIR/sub-mm SEDs in numerous ways. First, rather than being intrinsically red due to high redshifts ($z > 4$), it is likely that our 500 μm risers are artificially reddened in the *Herschel* SPIRE bands due to the fact that the successively larger beamsizes at longer wavelengths exacerbate the effects of blending (see e.g. Bussmann et al. 2015; Duivenvoorden et al. 2018). For example, Ma et al. (2019) and Montaña et al. (2021) estimate that ∼20 per cent and ∼25 per cent of their samples, respectively, would not pass the 500 μm riser selection criterion after accounting for the effects of blending. We additionally find that our SCUBA-2 observations may miss a significant fraction of the integrated flux density at 850 μm (particularly for Bootes15 and Bootes27) and that there may be additional faint sources contributing to the integrated FIR/sub-mm flux density that remain undetected in our SMA observations (particularly for Bootes27). The combination of missing flux at 850 μm and stronger blending at 500 μm would produce an artificially steep Rayleigh–Jeans tail, leading to significant difficulties in interpreting the resulting galaxy properties. Therefore, for a rigorous SED analysis, de-blending of the *Herschel* SPIRE flux densities will be necessary. However, due to the dearth of multiwavelength ancillary data in this region of the Bootes field and the uncertainty as to whether we have recovered all of the sub-mm sources associated with each region, accurate de-blending of the *Herschel* SPIRE flux density would be extremely challenging and could potentially produce misleading results. Given these difficulties, we do not attempt a rigorous SED fitting in this paper (although we do attempt some simple deblending, described later in this section), and instead we simply estimate the photometric redshifts of our 500 μm risers based on their integrated S_{250}/S_{350} versus S_{350}/S_{850} colours (Fig. 6). The purple and blue areas highlight regions in the colour–colour plot where $z \geq 2$ and $1 < z < 2$ DSFGs likely lie based on photometry from typical DSFG templates measured at various redshifts (see Cheng et al. 2019 for more details). For Bootes27, we calculate the FIR/sub-mm colours for both the total system, and each of the partially resolved sources associated with the SCUBA-2 850 μm detection by dividing the *Herschel* SPIRE flux density proportionally between the two components. These two components are shown as lighter red shapes in Fig. 6, but we find that both inhabit a similar space in the FIR/sub-mm colour–colour diagram to the total system.

As an independent estimate of the photometric redshift, we additionally run the MMPZ algorithm[5] (Casey 2020) which finds the most likely redshift at which a galaxy resides by determining where its FIR/mm SED is most consistent with the observed $L_{\rm IR}$–$\lambda_{\rm peak}$ relation, where $\lambda_{\rm peak}$ is the rest-frame wavelength at which the FIR/mm SED peaks (Lee et al. 2013; Strandet et al. 2016; Casey et al. 2018, 2021; Casey 2020). We use the integrated FIR photometry for each source, including the *Herschel* SPIRE and SCUBA-2 photometry, and obtain a photometric redshift PDF for each of our 500 μm risers. The full PDF for each source can be found in Appendix D. Based on the upper

[5]http://www.as.utexas.edu/~cmcasey/mmpz.html

Downloaded from academic.oup.com/mnras/article/519/1/709/6849985 by Imperial College of Science Technology and Medicine user on 19 October 2026

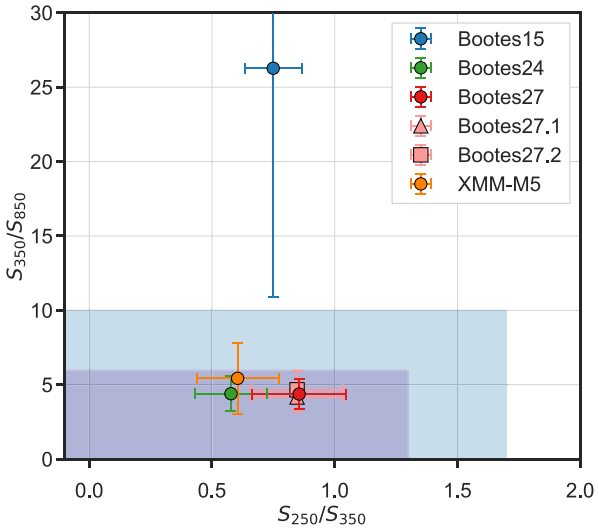


Figure 6. S_{250}/S_{350} versus S_{350}/S_{850} colour–colour diagram for our four 500 μm risers. The purple region in the lower left corner and the blue region surrounding it indicate likely colours for $z \geq 2$ and $1 < z < 2$ DSFGs, respectively. Bootes24, Bootes27, and XMM-M5 are all consistent with residing at $z \geq 2$, while Bootes15 remains unconstrained due to the poor SCUBA-2 photometry.

and lower 68 per cent credible intervals, we find likely photometric redshifts of $1.83^{+1.33}_{-1.80}$ for Bootes15, $3.03^{+1.02}_{-0.90}$ for Bootes24, $2.53^{+0.83}_{-0.70}$ for Bootes27, and $2.88^{+1.02}_{-0.90}$ for XMM-M5. These values are in good agreement with the FIR/sub-mm colours, and we infer that Bootes24, Bootes27, and XMM-M5 likely lie at $z \geq 2$. We note that the photometric redshift of Bootes15 remains essentially unconstrained due to the poor SCUBA-2 photometry.

We also attempt a simple deblending, using MMPZ to provide a rough estimate of the photometric redshift of the resolved sources associated with each 500 μm riser. For Bootes15 and Bootes24, we divide the *Herschel* SPIRE and SCUBA-2 photometry for the total systems proportionally based on the flux densities of the resolved SMA sources. For Bootes27, we divide the *Herschel* SPIRE flux proportionally between the two partially resolved components of the SCUBA-2 detection. We then run MMPZ once more on this naively deblended photometry. For the two deblended Bootes15 sources, we estimate photometric redshifts of $1.53^{+1.86}_{-1.50}$ and $1.53^{+1.95}_{-1.50}$, while for the two SCUBA-2 components associated with Bootes27, we estimate photometric redshifts of $2.78^{+0.65}_{-0.75}$ and $2.78^{+0.70}_{-0.75}$. The SMA flux densities of the two sources associated with Bootes24 are equal, and so we estimate a photometric redshift of $2.88^{+0.90}_{-0.90}$ for each. We include the full photometric redshift PDF for each of the resolved sources in Appendix D. We note that, in each of these cases, the photometric redshifts estimates for the resolved sources are very similar to those estimated based on the integrated flux densities of the 500 μm risers, and identical to each other, albeit with slightly different uncertainties.

4.3 Wider environment

4.3.1 *Overdensities of 850 μm sources*

To investigate the environments surrounding our 500 μm riser sources, we construct cumulative number counts based on the SCUBA-2 850 μm detections in the wider field. We construct these cumulative number counts in steps of 1 mJy based on the SCUBA-2 detections outlined in Table 4. We note that the 500 μm risers themselves are excluded as they were selected to lie within the maps. We apply an effective area correction to account for the variable noise in the SCUBA-2 maps. For each of our detected SCUBA-2 sources, we take the extracted flux density prior to deboosting and find the threshold RMS noise value above which the source could no longer be detected with SNR > 4. We then calculate the number of pixels in the map with a standard deviation below this threshold value and multiply by the area of one pixel to calculate the effective area (A_e) in square arcseconds over which the source could be detected to SNR >4. We convert this effective area into units of 'map size', where one map size is equal to the area of the 700 arcsec diameter circular region. Each source then effectively contributes $1/A_e$ to the cumulative number counts (Wang et al. 2017).

In order to determine whether there are overdensities of SMGs in our SCUBA-2 maps, we follow the analysis of Cheng et al. (2019) and compare our cumulative number counts to the expected number of field counts from S2CLS. We first convert the cumulative number counts per square degree from table 4 in Geach et al. (2017) to cumulative number counts per map size by multiplying by our map area in square degrees. In Fig. 7, we compare the cumulative number counts from S2CLS with our SCUBA-2 maps. We then quantify the overdensity at each flux density level using Poisson statistics. We first take the observed cumulative number counts above each flux density level and calculate the probability of observing that number of sources using the Poisson probability mass function

$$f(k) = \exp(-\mu)\frac{\mu^k}{k!}, \tag{2}$$

where k represents the number of observed counts and μ represents the expected number of counts from S2CLS. We then calculate the overdensity level using the equation

$$\delta = \frac{k-\mu}{\sqrt{\mu}}, \tag{3}$$

as well as calculating an uncertainty in this overdensity by propagating the errors on the observed and expected counts. We additionally include the reliability estimates from the jackknife maps (see Section 3.2) in the uncertainties associated with the overdensity estimates.

We find that Bootes15 hosts an overdensity of 8.6 ± 3.5 of SMGs brighter than 8 mJy, while Bootes24 shows a more marginal 5.8 ± 3.5 overdensity of SMGs brighter than 8 mJy. The probabilities of observing these numbers of sources in a random field are 2.8×10^{-7} and 1.1×10^{-4}, respectively. While Bootes27 appears to harbour a large overdensity of faint ($S_{850} > 4$ mJy) sources, this overdensity is driven by a single source with a deboosted flux density of ∼4.9 mJy that would only be detected to SNR > 4 in ∼3 per cent of the total map area. This results in a large effective area correction and hence an artificially high overdensity value. If this single source is removed, then we do not observe any overdensity in the Bootes27 region. For XMM-M5, we find an overdensity of 9.3 ± 6.5 of sources brighter than 9 mJy compared to the field counts, with a probability of observing this number of counts in a blank field of $\sim 2 \times 10^{-6}$. This analysis therefore identifies Bootes15, Bootes24, and XMM-M5 as regions plausibly containing overdensities of bright SCUBA-2 850 μm sources.

4.3.2 *Cross-matching with HerMES sources*

To investigate these potential overdensities further, we then cross-match the SCUBA-2 850 μm detected sources with the HerMES (Oliver et al. 2012) catalogues. We use the optimum search radius of 9

Downloaded from academic.oup.com/mnras/article/519/1/709/6849985 by Imperial College of Science Technology and Medicine user on 19 October 2026

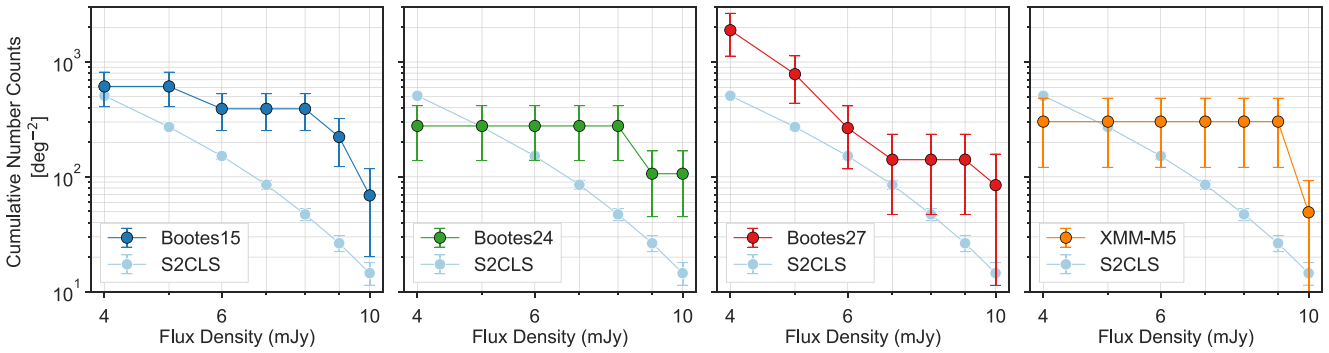


Figure 7. Cumulative number counts for the four 500 μm riser fields, plotted alongside the expected cumulative number counts in the field from S2CLS. The Bootes15, Bootes24, and XMM-M5 fields are overdense in bright ($S_{850} \gtrsim 8$ mJy) sub-mm sources.

arcsec identified by Cheng et al. (2019), matching half of the FWHM of the *Herschel* SPIRE 250 μm beam, such that any SCUBA-2 source within 9 arcsec of a source in the HerMES catalogue is considered a potential companion. Through this cross-matching process we find that 3/9 (33 per cent), 2/4 (50 per cent), 3/7 (43 per cent), and 3/5 (60 per cent) SCUBA-2 detections have *Herschel* counterparts for the Bootes15, Bootes24, Bootes27, and XMM-M5 fields, respectively. These numbers exclude the 500 μm risers themselves. The positions and FIR/sub-mm photometry for each of these sources can be found in Table 4. In Fig. 8 we present the S_{250}/S_{350} versus S_{350}/S_{850} colours for both the 500 μm risers and the SCUBA-2 detections, while in Fig. 9 we plot their photometric redshifts and associated errors as estimated by MMPZ based on their *Herschel* and SCUBA-2 photometry. The full photometric redshift PDFs from MMPZ can be found in Appendix D.

The photometric redshift of Bootes15 is essentially unconstrained due to its poor SCUBA-2 photometry. However, the three SCUBA-2 detected sources with HerMES counterparts in the Bootes15 field have FIR/sub-mm colours consistent with $z \geq 2$, although MMPZ has trouble constraining the redshifts of two of them. Both Bootes24 and its companion SCUBA-2 detections have colours consistent with $z \geq 2$, and MMPZ places these sources at $z \sim 2$–3 (although Bootes24 itself suffers from larger error bars, placing it in the range$z \sim 2$–4). The FIR/sub-mm colours of sources in the Bootes27 region suggest that they are spread over a large range in redshift and so are unlikely to be physically associated, and this is supported by the results of MMPZ. The XMM-M5 field is plausibly overdense in FIR/sub-mm bright sources, and their colours suggest that they all reside at $z \geq 2$. The MMPZ results, however, offer a somewhat more complicated picture, placing two of the SCUBA-2 detections at $z \sim 1.5$–2 and the third (XMM-M5.SCUBA1) at $z \sim 4$. This is consistent with the *Herschel* SPIRE photometry for XMM-M5.SCUBA1 which satisfies the colour criteria for a 500 μm riser (see Table 4).

5 DISCUSSION

5.1 Multiplicities

We find evidence of multiplicity in three of our four 500 μm risers. Bootes15 and Bootes24 each breaking up into two resolved sources in the high-resolution SMA maps, while Bootes27 is clearly comprised of two partially resolved sources in the SCUBA-2 imaging. This builds on the work of G20, who found that ∼35 per cent of bright ($S_{500} > 60$ mJy) 500 μm risers are multiples, while fainter 500 μm risers are also blends more often than expected. These conclusions were reached based on the assumption that the 12 500-μm risers without SMA detections in their follow-up observations are comprised of multiple DSFGs that were individually too faint to be detected in their SMA maps, but all of which contribute to the bright *Herschel* source. By identifying evidence of multiplicity in three out of four of these 500 μm risers, our observations support this conclusion. It is worth noting that, while we do observe evidence of multiplicity, we currently do not detect the high multiplicities of ≥3 that were predicted by G20 for these 500 μm risers. However, given the discrepancies between the *Herschel*, SCUBA-2, and SMA photometry, we cannot rule out the possibility of additional faint counterparts lying below our current detection limits. In the following sections, we discuss Bootes15 and Bootes27, which are particularly interesting cases, in more detail.

5.1.1 *Bootes15*

Fig. 4 demonstrates that the SMA and SCUBA-2 photometry for Bootes15 are in good agreement within the rather large 850 μm error bars, but Fig. 5 indicates that its 850 μm flux density is much lower than we would expect based on its 500 μm flux density. The SCUBA-2 observations reach a depth of 2.2 mJy, and so it is reasonable to expect that at least part of this discrepancy could be due to the SCUBA-2 observations missing a significant fraction of the total 850 μm flux density in the system. This missing flux density could be in the form of extended, diffuse emission or additional point-like sources lying below our SCUBA-2 detection threshold. However, if we assume that the 850 μm flux density is underestimated and in reality is more in line with similarly bright *Herschel* sources in the S2CLS and STUDIES samples (e.g. ≳10 mJy at 850 μm), this would introduce a significant discrepancy between the SMA and SCUBA-2 photometry, similar to the discrepancy we observe in Bootes27. We therefore suggest that this discrepancy is caused not only by missing 850 μm flux density in the SCUBA-2 observations, but also in part by faint sources lying below both our SMA and SCUBA-2 detection limits. Additional undetected sources would not only account for the faint SMA and SCUBA-2 flux densities, but the effects of blending would also artificially redden the *Herschel* SPIRE photometry. Bussmann et al. (2015) find that blending can have a significant effect on the FIR/sub-mm colours of bright *Herschel* sources. For example, blends of three sources can boost the S_{500}/S_{350} colours of bright *Herschel* sources by as much as ∼1.8 times the deblended colours. This interpretation can therefore simultaneously account for the bright *Herschel* SPIRE source associated with Bootes15, its red *Herschel* colours, and its unexpectedly faint SCUBA-2 and SMA photometry.

Downloaded from academic.oup.com/mnras/article/519/1/709/6849985 by Imperial College of Science Technology and Medicine user on 19 October 2026

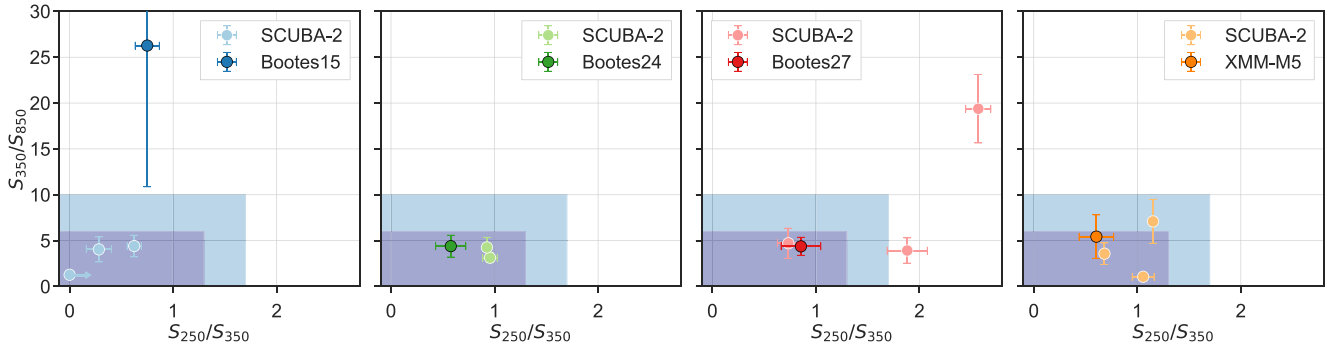


Figure 8. The S_{250}/S_{350} versus S_{350}/S_{850} FIR/sub-mm colours for our four 500 μm risers (dark points) alongside the SNR > 4 detections in the SCUBA-2 850 μm maps with *Herschel* counterparts (light points). The purple region in the lower left corner, and the blue region surrounding it, indicate likely colours for $z \geq 2$ and $1 < z < 2$ DSFGs, respectively. These plots demonstrate that the overdensities associated with Bootes24 and XMM-M5 are potentially physically associated at $z \geq 2$.

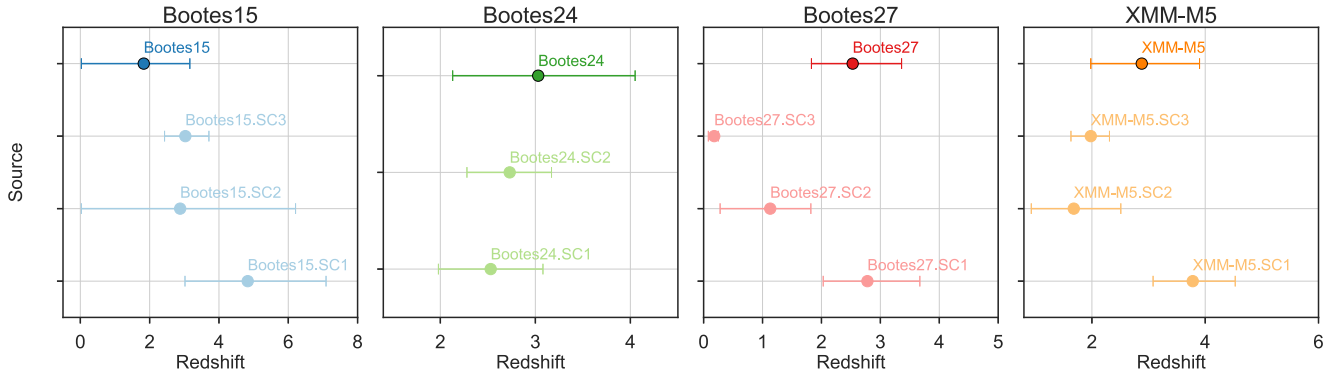


Figure 9. The photometric redshifts for our 500 μm risers and SCUBA-2 SNR > 4 detected sources estimated by MMPZ. Similarly to the FIR/sub-mm colours, we find that the Bootes24 region is consistent with containing a physically associated overdensity of bright DSFGs, with well-constrained photometric redshifts placing the surrounding SMGs at $z \approx 2$–3, and Bootes24 itself at $z \approx 2$–4. While the photometric redshift of XMM-M5 does overlap with those of the bright SCUBA-2 sources, there is a larger range of photometric redshifts, indicating that this region may be somewhat more complex. The DSFGs associated with Bootes15 do not have well-constrained photometric redshifts, and the bright SCUBA-2 sources in the Bootes27 region are likely unassociated with each other.

5.1.2 Bootes27

Bootes27 is another interesting case study. The SCUBA-2 contours show two partially resolved sources, a Southern component coincident with a single, much fainter SMA source, and a Northern component with no apparent counterpart in the SMA images. Moreover, even excluding the partially resolved Northern SCUBA-2 component, the brighter Southern component has a deboosted flux density of 6.9 ± 1.3 mJy, significantly larger than the 1.9 ± 0.4 mJy resolved SMA source associated with it. We also note that the single resolved SMA source is slightly offset from the brightest pixel in the SCUBA-2 maps. There are two other marginal SMA detections, one of which is coincident with the Northern component of the SCUBA-2 detection. The other is offset from the detected SCUBA-2 850 μm emission by ∼10 arcsec and remains undetected at 850 μm. We interpret these results as evidence of additional faint sources lying below even our deeper SMA detection threshold.

We can make a rough estimate of the number of sources that likely remain undetected in Bootes27 by comparing the integrated flux density from the SCUBA-2 observations to the resolved flux density from the SMA observations. The dirty map for Bootes27 has a 1σ RMS noise of ∼0.29 mJy beam^{-1}, so any source with a flux density of less than ∼1.2 mJy would fall below our 4.1σ detection threshold. The single resolved SMA source has a flux density of 1.9 ± 0.4 mJy. Based on the integrated SCUBA-2 flux density of 10.1 ± 1.6 mJy, we require at least 2.2 mJy of additional flux density in our SMA maps to avoid a 3σ tension between the SMA and SCUBA-2 photometry, corresponding to at least two additional faint sources lying below our SMA detection threshold. We note that the marginally detected component associated with the Northern component of Bootes27 has a flux density of 2.9 ± 0.9 mJy corrected for the response of the primary beam, and as such could ease the tension between these flux density values. Alternatively, if we take the flux density estimates at face value, the SMA observations miss 8.2 ± 1.6 mJy of flux density, and we would therefore require approximately six to nine undetected SMA sources contributing to the total SCUBA-2 flux density. Such a high multiplicity would make Bootes27 a candidate high-redshift protocluster core, potentially similar to those discovered by Miller et al. (2018) and Oteo et al. (2018). We note that the ancillary *Spitzer* IRAC data for Bootes27 show approximately seven individual sources detected to >3σ at 8.0 μm, approximately three of which remain completely undetected at 4.5 μm, indicating that there may be additional, extremely red sources contributing to the SCUBA-2 flux density that are undetected in the SMA map. A more comprehensive, multiwavelength analysis of Bootes27 will be presented in a future paper.

Downloaded from academic.oup.com/mnras/article/519/1/709/6849985 by Imperial College of Science Technology and Medicine user on 19 October 2026

5.2 Photometric redshifts

Based on their integrated FIR/sub-mm colours in Fig. 6, we find that our 500 μm risers likely lie at $z \geq 2$, excluding Bootes15 whose FIR/sub-mm colours remain poorly constrained due to the uncertain 850 μm photometry. This result is corroborated by MMPZ, which indicates that these 500 μm risers likely lie at $z \sim 2$–4. As well as being effective at selecting intrinsically red, high-redshift DSFGs, the 500 μm riser selection criterion will also naturally include some fraction of intermediate redshift systems that are artificially reddened by the blending of multiple sources at moderately large separations. For example, Montaña et al. (2021) find in their sample of ∼100 500-μm risers that the photometric redshift distribution of those that resolve into multiple components is skewed towards lower redshifts, with a slightly lower median redshift ($z_{\rm med} = 3.5$ versus $z_{\rm med} = 3.8$) and a higher fraction residing at lower redshifts (27 per cent at $z_{\rm phot} < 3$ versus 10 per cent) compared to single systems. We find that our 500 μm risers typically fall into the category of multiple systems at moderate redshifts and, based on their FIR/sub-mm flux densities and intermediate photometric redshifts, we would expect them to be examples of Hyper-Luminous Infrared Galaxies (HLIRGS: $L_{\rm FIR} > 10^{13}\,{\rm L}_{\odot}$), similar to those discussed in G20.

5.3 Environments

Our SCUBA-2 850 μm observations map out sub-mm emission over a >10 arcmin region surrounding our 500 μm risers, and are therefore extremely useful for characterizing their environments. DSFGs have the potential to be used as signposts for overdensities of galaxies in the early Universe, allowing us to identify the potential progenitors of massive, local galaxy clusters. We find that, while the Bootes27 region is consistent with the expected number of field counts from S2CLS, Bootes15, Bootes24, and XMM-M5 are all consistent with lying in overdensities of SMGs with 850 μm flux densities greater than ∼8 mJy. We do note, however, that the error bars on these overdensity values for Bootes24 and XMM-M5 are rather large, with only a very marginal overdensity at the lower limit. This result is interesting as we would not necessarily expect our 500 μm risers to be effective tracers of high-redshift galaxy overdensities – based on the clustering analysis of SMGs from the ALESS survey, García-Vergara et al. (2020) find that only the brightest SMGs ($S_{870} >$ 5–6 mJy) should trace massive structures at $z \sim 2$, while our sources are significantly fainter than this in the resolved SMA maps. Without spectroscopic redshifts for the SCUBA-2 sources we cannot say with certainty whether these overdensities are physically associated structures or simply chance line-of-sight projections of bright sub-mm sources. In the absence of spectroscopic data, we must rely on photometric redshifts estimated from FIR/sub-mm colour–colour diagrams and the MMPZ algorithm. From Figs 8 and 9, we infer that the marginal overdensity associated with Bootes24 could be physically associated with the FIR/sub-mm colours placing the sources at $z \geq 2$, and MMPZ placing them at $z \sim 2$–4. For the Bootes15 field, improvements in the FIR/sub-mm photometry are required to better constrain the photometric redshifts of the detected sources, while the sources in the Bootes27 field likely reside at very different redshifts. The SCUBA-2 detections in the XMM-M5 field could represent an overdensity of SMGs, and their colours suggest that they are all at $z \geq 2$, but MMPZ places two of these sources at $z \sim$ 1.5–2, and the third at $z \sim 4$. This overdensity is therefore less likely to be a physically associated structure than Bootes24. Additional observations providing improved photometry and/or spectroscopic redshifts for these sources will be required to conclude with certainty whether they are physically associated structures.

5.4 Comparison to predictions for bright *Herschel* sources

5.4.1 *Brightest galaxy fraction*

We first compare the flux distributions of the resolved SMA sources in our 500 μm risers to the literature. Béthermin et al. (2017), based on their simulations, predict that the brightest galaxy should contribute ∼60 per cent of the total 500 μm flux density. Similarly, Donevski et al. (2018) find that the brightest galaxy inside the *Herschel* beam for their simulated SPIRE data contributes on average 75 per cent and 64 per cent at 250 and 500 μm, respectively. Montaña et al. (2021) find that the brightest component contributes on average 50–75 per cent of the total flux density at 1.1 mm, while Ma et al. (2019) find that the brightest ALMA source contributes on average 41–80 per cent of the total ALMA flux density and 15–59 per cent of the total SCUBA-2/LABOCA flux density at a similar wavelength.

We find that the brightest SMA component in Bootes15 contributes 56 ± 12 per cent to the total SMA flux density, and 69 ± 41 per cent of the integrated SCUBA-2 850 μm flux density. For Bootes24 the brightest SMA component contributes 50 ± 9 per cent to the total SMA flux density, but just 30 ± 8 per cent to the integrated SCUBA-2 flux density at a similar wavelength. For these two 500 μm micron risers that resolve into multiple SMA components, the brightest galaxy fraction is in good agreement with the values of ≈ 50–60 per cent found by G20 for the four 500 μm risers in their sample that break up into multiple SMA components. For Bootes27, the single resolved SMA component contributes just 19 ± 4 per cent of the integrated SCUBA-2 850 μm flux density. These values are in good agreement with Ma et al. (2019), and indicate that for Bootes24 and Bootes27, we may not recover the total sub-mm flux density.

5.4.2 *Multiplicity fraction*

Our results support the conclusions of G20, who find that ∼ 35 per cent of bright ($S_{500} >$ 60 mJy) 500 μm risers, and ∼ 60 per cent of faint ($S_{500} <$ 60 mJy) 500 μm risers are multiples, although we note that these observations were somewhat inhomogeneous, using a variety of frequencies (ranging from 231 to 346 GHz) and configurations, with a mixture of full tracks, partial tracks, and track sharing, resulting in a range of angular resolutions (with an average beam FWHM of 2.5 ± 0.8 arcsec) and depths (0.5–2.9 mJy beam^{-1}).

Oteo et al. (2017) provide high-resolution (∼0.12 arcsec) ALMA follow-up observations at 870 μm for 44 ultra-red DSFGs from HerMES and H-ATLAS with $S_{500}/S_{250} > 1.5$ and $S_{500}/S_{350} >$ 1.0, reaching 1σ RMS sensitivities of 0.1 mJy beam^{-1}. They find that, in total, ≈ 39 per cent resolve into multiple components and, more specifically, ≈ 22 per cent of bright ($S_{500} >$ 60 mJy) and ≈ 65 per cent of faint ($S_{500} \leq$ 60 mJy) sources in their sample resolve into multiple components.

Béthermin et al. (2017) produce an FIR to submillimetre simulation of the extragalactic sky based on a galaxy evolution model with two star-formation modes. They extract sources from maps based on these observations to investigate the effects that the limited angular resolution of single-dish instruments has on observations in the FIR/sub-mm. They predict that all *Herschel* sources brighter than 60 mJy at 500 μm should be individual, lensed sources, while ∼40 per cent of sources fainter than 60 mJy at 500 μm should be blended.

Downloaded from academic.oup.com/mnras/article/519/1/709/6849985 by Imperial College of Science Technology and Medicine user on 19 October 2026

In their compilation of 63 500-μm risers, Ma et al. (2019) estimate a multiplicity fraction of ∼27 per cent based on numerous follow-up observations with NOEMA, ALMA, and the SMA, although these studies reach various depths and angular resolutions, as well as probing much fainter 500 μm flux densities. This multiplicity fraction rises to ∼39 per cent when sources showing evidence of strong gravitational lensing are removed.

Montaña et al. (2021) carry out 1.1 mm LMT/AzTEC observations of ∼100 500-μm risers with $S_{500} \approx 35$–80 mJy, achieving an average beam FWHM of 9.6 ± 0.5 arcsec and 1σ RMS sensitivities of ≈0.7–2.8 mJy. They find that ∼9 per cent show direct evidence of multiplicity, rising to ∼23 per cent if 500 μm risers which display evidence of multiplicity but are slightly below their detection threshold are included, and up to ∼50 per cent if 500 μm risers without counterparts in their higher resolution observations are assumed to be multiple sources. This is considered an extreme scenario as a higher dust spectral emissivity index β could also render some of their sources undetectable at 1.1 mm, but our observations of 500 μm risers without counterparts in previous, high-resolution follow-up observations indicate that a significant fraction of these non-detections could be multiple systems. For the 12 sources in their sample with $S_{500} > 60$ mJy, two break up into multiple components and three show no counterparts in their higher resolution images, indicating a multiplicity of ≈ 17–42 per cent. However, the larger beamsize of their observations compared to Oteo et al. (2017) and G20 probe multiplicity on a significantly different scale, such that smaller scale multiplicities would likely be classified as individual sources. They estimate a correction factor of ∼10 per cent accounting for multiple systems separated by distances much smaller than their 9.6 ± 0.5 arcsec beamsize, bringing the multiplicity fraction up to $\gtrsim$ 18 per cent in the conservative case and ∼60 per cent in the extreme case.

We find that our three Bootes sources all show some evidence of multiplicity, with all three resolving into multiple sources in either the SMA or SCUBA-2 follow-up observations. This result supports the conclusions of G20 and, by extension, is in good agreement with the multiplicity fractions for 500 μm risers quoted by Oteo et al. (2017), despite their ALMA observations achieving significantly better sensitivities and angular resolutions. These results are also in reasonably good agreement with the more extreme scenario in Montaña et al. (2021), and well within the range of potential multiplicity fractions of the brightest ($S_{500} > 60$ mJy) sources in their sample.

These multiplicity fractions indicate that 500 μm risers are a much more diverse population than predicted by the simulations of Béthermin et al. (2017). We suggest that this disparity could be related to the source extraction algorithm used in their simulations. Béthermin et al. (2017) extract sources from their simulated *Herschel* SPIRE maps using the FAST-PHOT algorithm, with the source positions at 24 μm used as a positional prior. They do note, however, that such algorithms do not converge when there are numerous sources within the same beam due to degeneracies in the contributions of each source to the total integrated flux density. As such, they only keep the brightest 24 μm source within a radius of half of the FWHM of the *Herschel* SPIRE instrument in their list of positional priors. Of the four brightest 500 μm risers that remained undetected in G20, our results suggest that two break up into two sources, while Bootes27 is likely comprised of even more individual galaxies. It is possible therefore that the fainter sources not detected in G20 that are yet to be followed up in detail may similarly break up into highly multiple systems. Such systems with multiple sources clustered within the *Herschel* beam may have been missed by the FAST-PHOT algorithm by only keeping the brightest 24 μm source within the SPIRE beam, leading to an underestimate of the number of 500 μm risers comprised of blends of DSFGs. Such a scenario is in agreement with our estimated brightest galaxy fractions which, for Bootes24 and Bootes27, are significantly lower than those estimated by Béthermin et al. (2017).

5.4.3 Comparison to known protocluster cores

We can also compare these values to the flux density distributions of known high-z protocluster cores, such as the Distant Red Core (DRC: Oteo et al. 2018) and SPT2349-56 (Miller et al. 2018). For the DRC, we focus on the ALMA 2 mm follow-up observations carried out by Oteo et al. (2018) which targeted the bright 500 μm riser observed with *Herschel*, SCUBA-2 and LABOCA by Ivison et al. (2016). The ALMA observations reached depths of ∼6 μJy beam^{-1} with a synthesized beam FWHM of 1.68 arcsec × 1.54 arcsec. The LABOCA source representing the central core of the DRC is extended of the order of ∼1 arcmin, with the ALMA follow-up observations revealing 11 individual DSFGs associated with the system, typically separated by ≈5–10 arcsec. We assume that these observations recover the full 2 mm flux density of the system and, as such, estimate the total 2 mm flux density by simply summing the flux densities of the individual components. The fractional contribution of each source is then simply its 2 mm flux density divided by the total 2 mm flux density of the system.

For SPT2349-56, we use the flux densities extracted from the ALMA 850 μm continuum maps based on the [CII] map channels with no line emission (Hill et al. 2020). These follow-up observations focused on the core of SPT2349-56 which was found to be extremely bright at 870 μm with LABOCA and at 2 mm with the South Pole Telescope, yielding ≈22 sources within a circle of radius ≈13 arcsec. We estimate the fractional contribution of each 850 μm source similarly to the method for the DRC.

We note that the separations found in the DRC are somewhat smaller than the ≈15 arcsec separations between our resolved SMA sources, and that the LABOCA source is extended over a larger scale than our SCUBA-2 observations. Similarly, we note that there are ≈12 sources within a 10 arcsec × 10 arcsec box near the centre of SPT2349-56 and, as such, the DSFGs are in much closer proximity than in our multiple systems, although the angular scale of the core is more comparable with the scale of Bootes24 and Bootes27 in the SCUBA-2 observations. As such, we make the following comparisons for illustrative purposes only, and they should not be considered as robustly similar systems based on the current data.

In Fig. 10, we plot the contribution of each of the 10 brightest resolved sources associated with the protocluster cores to the total flux density in the aforementioned bands. For our 500 μm risers, we plot the contribution of each of the resolved SMA sources to the integrated SCUBA-2 850 μm flux density, and estimate the uncertainties in these contributions by adding in quadrature the errors in the resolved SMA and integrated SCUBA-2 flux densities. We note that, given the uncertainties in the estimated flux densities and the small separation in wavelength, we do not extrapolate the 870 μm SMA flux densities down to 850 μm values, but rather assume that the values will be approximately the same. Furthermore, note that we exclude XMM-M5 from this plot, as the SMA and SCUBA-2 observations were taken at very different wavelengths.

For Bootes15, the contribution of each SMA source to the total SCUBA-2 flux density is poorly constrained, primarily due to the large uncertainties in the 850 μm photometry. In total, we

Downloaded from academic.oup.com/mnras/article/519/1/709/6849985 by Imperial College of Science Technology and Medicine user on 19 October 2026

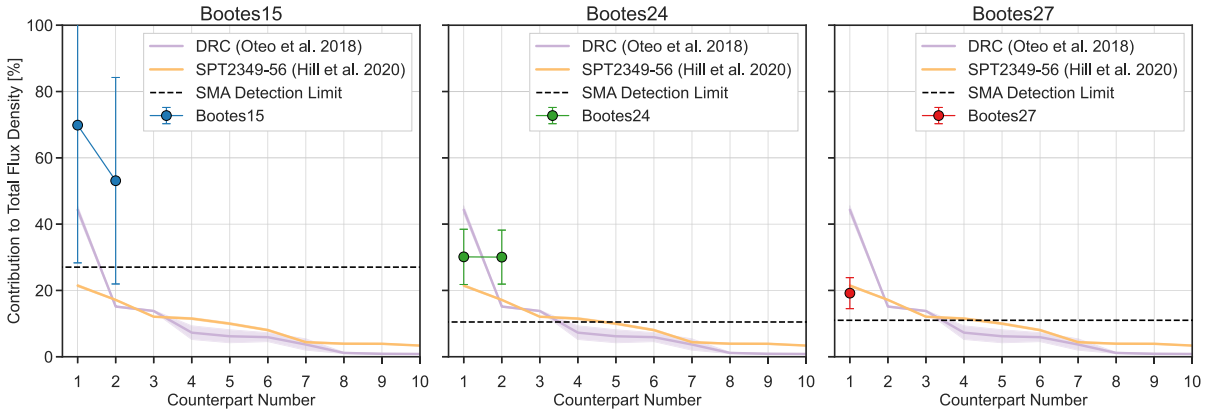


Figure 10. The relative contributions of each of our SMA detections to the total integrated SCUBA-2 850 μm flux density. The orange and purple lines show the flux density distributions of the DRC and SPT2349-56 protoclusters, respectively, while the black dashed lines show the 4.1σ detection limits in our dirty SMA maps. The contribution of each SMA source to the integrated SCUBA-2 flux density of Bootes15 remains poorly constrained. The SMA sources associated with Bootes24 and Bootes27 recover 60 ± 15 per cent and 19 ± 4 per cent of the total integrated SCUBA-2 flux density and so there may be additional sources residing below our SMA detection limits. However, if further sources do reside below our detection threshold, they likely follow a different flux density distribution to the DRC and SPT2349-56 protoclusters.

estimate that the SMA observations recover 123 ± 73 per cent of the SCUBA-2 observations. However, as previously discussed, it is likely that some fraction of the total SCUBA-2 flux density is missed by our observations. The two SMA sources associated with Bootes24 recover 60 ± 15 per cent of the total SCUBA-2 flux density, shared equally between the two resolved sources. Therefore, the combined contribution from the two brightest sources is in good agreement with the two brightest sources in the DRC, which similarly contribute ∼60 per cent to the total flux density of the system. However, the flux density is shared much more unequally between the two brightest sources in the DRC. If there were additional sub-mm sources contributing to Bootes24, we would expect to detect one extra source in our SMA observations if they were to follow a DRC-like flux density distribution. Alternatively, we would expect to detect the brightest four to five sources if they were to follow a SPT2349-56-like flux density distribution. For Bootes27, the single resolved SMA source associated with the observed SCUBA-2 emission contributes just 19 ± 4 per cent to the integrated 850 μm flux density. This is similar to the ∼22 per cent contribution to the total system from the brightest source in SPT2349-56. However, if Bootes27 were to represent a protocluster core with a similar flux density distribution to SPT2349-56, we would similarly expect to detect the brightest four to five components, whereas we only detect a single source associated with the 850 μm emission.

We infer that Bootes24 and Bootes27 may contain additional, faint sources lying below our SMA detection threshold that contribute to the total integrated SCUBA-2 flux density. However, it seems that this flux density must be distributed between its members differently to known high-redshift protocluster cores, with each of the fainter members individually contributing significantly less to the total sub-mm flux density than expected.

6 CONCLUSIONS

We have presented *Herschel*, SMA, and SCUBA-2 observations of four 500 μm risers from the HerMES survey. These sources were selected based on their red *Herschel* SPIRE colours, but remained undetected in previous high-resolution follow-up observations conducted by G20. The previous results indicated that they were likely comprised of multiple DSFGs that individually were faint enough to remain undetected in their high-resolution SMA observations, but each contributing to a large integrated flux density when smoothed over the *Herschel* SPIRE beamsize. In our deeper FIR/sub-mm observations, each source is detected to >3σ in the SCUBA-2 maps, and there is at least one >4.1σ detection in each of the SMA maps. Our findings can be summarized as follows.

(i) We find evidence of multiplicity in three out of four 500 μm risers. Bootes15 and Bootes24 each break up into two faint sources in the high-resolution SMA images, while Bootes27 and XMM-M5 resolve into a single SMA source. Bootes27 is comprised of two, partially resolved SCUBA-2 detections, one of which has no apparent SMA counterpart, indicating that there may be further faint DSFGs lying below the SMA detection threshold. This is in line with the results of G20 who found (assuming that their 500 μm risers without SMA counterparts are sources with high multiplicities) that ∼35 per cent of bright (S_{500} > 60 mJy) 500 μm risers and ∼60 per cent of faint (S_{500} < 60 mJy) 500 μm risers are multiples. By providing deeper SMA follow-up observations of these 500 μm risers, we confirm that they are likely comprised of multiple faint components. These results indicate that the 500 μm riser population is likely significantly more diverse than expected. We do note, however, that only three of the 500 μm risers that remained undetected in G20 have been confirmed as multiple systems, and so the fraction of faint 500 μm that resolve into multiple galaxies could still be less than 60 per cent.

(ii) For the three 500 μm risers in the Bootes field, the SMA observations recover 123 ± 73 per cent, 60 ± 15 per cent, and 19 ± 4 per cent of the integrated SCUBA-2 flux density indicating that, for Bootes24 and Bootes27, there may be additional, faint sources below the current SMA detection limit, but contributing to the integrated SCUBA-2 flux density. In particular, for Bootes27, there is a >3σ disparity between the resolved SMA and integrated SCUBA-2 flux densities. We estimate that at least three additional faint sources are required to recover the total SCUBA-2 flux density. We note that a second associated with the Northern component of Bootes27 is marginally detected to 3.3σ in the dirty map, and could significantly ease this tension. We conclude that Bootes24 and Bootes27 could be

Downloaded from academic.oup.com/mnras/article/519/1/709/6849985 by Imperial College of Science Technology and Medicine user on 19 October 2026

examples of dense, protocluster cores of DSFGs, only a handful of which have been discovered to date.

(iii) We estimate the photometric redshifts of our 500 μm risers using their FIR/sub-mm colours, as well as the MMPZ algorithm. While the photometric redshift of Bootes15 remains poorly constrained, Bootes24, Bootes27, and XMM-M5 all likely lie at $z \geq 2$. Dividing the integrated flux density from *Herschel* SPIRE proportionally between the resolved components and running the MMPZ algorithm yields similar photometric redshift estimates. This is consistent with the interpretation that the 500 μm riser selection criterion recover both intrinsically red sources at $z > 4$ and artificially red, multiple systems at more moderate redshifts. Based on their FIR flux densities and photometric redshifts, we expect our sources to be HLIRGs, similar to those in the G20 sample.

(iv) By comparing the cumulative number counts of SNR > 4 detections in the SCUBA-2 850 μm maps with the expected number of field counts from the SCUBA-2 Cosmology Legacy Survey, we find that Bootes15, Bootes24, and XMM-M5 lie in regions with overdensities of 8.6 ± 3.5, 5.8 ± 3.5, and 9.3 ± 6.5 of bright ($\gtrsim$8 mJy) SMGs, respectively. For those SCUBA-2 detections that have *Herschel* SPIRE counterparts, we estimate photometric redshifts based on their FIR/sub-mm photometry. We find that the overdensity associated with Bootes24 could feasibly be physically associated, while Bootes15 and XMM-M5 are more likely to be chance line-of-sight arrangements of sources.

(v) We compare the inferred multiplicity fractions of 500 μm risers from G20 to similar studies in the literature, finding that they are in good agreement with Oteo et al. (2017) and with the more extreme scenarios in Montaña et al. (2021). The brightest galaxy fraction for Bootes15 and Bootes24 is similar to the other multiple systems revealed by the SMA observations of G20. We also find that the brightest SMA component of Bootes24 and Bootes27 contributes a similar amount to the total integrated SCUBA-2 flux density as the brightest resolved source associated with the 500 μm risers in the Ma et al. (2019) sample.

(vi) We also compare the flux density distributions of our resolved SMA sources to those of known protocluster cores. We find that, while the SMA sources associated with Bootes24 and Bootes27 only recover a fraction of the total sub-mm flux density, we would have expected to detect the brightest four to five components if the multiple systems followed a similar flux density distribution to SPT2349-56, or the brightest three components if they followed a similar flux density distribution to the DRC. Therefore, if these 500 μm risers are examples of dense protocluster cores, they likely follow a different flux density distribution to known, high-z protocluster cores.

We therefore find that our 500 μm risers are typically comprised of multiple DSFGs and may represent examples of high-redshift protocluster cores. However, additional follow-up observations will be required to confirm the nature of these sources, and there are a number of available avenues that these observations could take. Deeper sub-mm continuum/spectroscopic observations with NOEMA will likely be required to determine if there are any additional, faint, point-like sources below our current SMA detection limits that contribute to the integrated SCUBA-2 flux (and if these sources are physically associated), particularly for Bootes27 where our SMA observations currently recover only a fraction of the total 850 μm flux density. Alternatively, deep optical/NIR follow-up observations would allow us to accurately deblend the *Herschel* SPIRE flux density, from which we could attempt a rigorous SED fitting for each of the resolved components and estimate galaxy properties such as SFR and stellar mass. Finally, additional spectroscopic follow-up observations for sources in the wider field would allow us to conclude whether any larger scale overdensities in these regions represent physically associated structures.

ACKNOWLEDGEMENTS

The authors wish to thank the anonymous referee, whose detailed and insightful comments have vastly improved this manuscript.

The authors wish to recognize and acknowledge the very significant cultural role and reverence that the summit of Mauna Kea has always had within the indigenous Hawaiian community. We are most fortunate to have the opportunity to conduct observations from this mountain.

The Submillimeter Array is a joint project between the Smithsonian Astrophysical Observatory and the Academia Sinica Institute of Astronomy and Astrophysics and is funded by the Smithsonian Institution and the Academia Sinica.

The James Clerk Maxwell Telescope is operated by the East Asian Observatory on behalf of The National Astronomical Observatory of Japan; Academia Sinica Institute of Astronomy and Astrophysics; the Korea Astronomy and Space Science Institute; Center for Astronomical Mega-Science (as well as the National Key R&D Program of China with No. 2017YFA0402700). Additional funding support is provided by the Science and Technology Facilities Council of the United Kingdom and participating universities and organizations in the United Kingdom and Canada.

This research has used data from HerMES project (http://hermes.sussex.ac.uk/). HerMES is a Herschel Key Programme utilizing Guaranteed Time from the SPIRE instrument team, ESAC scientists, and a mission scientist.The HerMES data were accessed through the Herschel Database in Marseille (HeDaM – http://hedam.lam.fr) operated by CeSAM and hosted by the Laboratoire d'Astrophysique de Marseille.

This research used the facilities of the Canadian Astronomy Data Centre operated by the National Research Council of Canada with the support of the Canadian Space Agency.

This research made use of APLPY, an open-source plotting package for Python hosted at http://aplpy.github.com. This research used ASTROPY, a community-developed core Python package for Astronomy (Astropy Collaboration 2013, 2018). This research used PHOTUTILS, an Astropy package for detection and photometry of astronomical sources (Bradley et al. 2021). This research used the Starlink Table/VOTable Processing Software TOPCAT (Taylor 2005).

JC acknowledges support from the Science and Technology Facilities Council (grant number ST/S505432/1). IP-F acknowledges support from the Spanish State Research Agency (AEI) under grant number PID2019-105552RB- C43.

DATA AVAILABILITY

The data underlying this article will be shared on reasonable request to the corresponding author.

REFERENCES

Alexander D. M., Bauer F. E., Chapman S. C., Smail I., Blain A. W., Brandt W. N., Ivison R. J., 2005, ApJ, 632, 736
Álvarez Crespo N., Smolić V., Finoguenov A., Barrufet L., Aravena M., 2021, A&A, 646, A174
Asboth V. et al., 2016, MNRAS, 462, 1989
Astropy Collaboration, 2013, A&A, 558, A33
Astropy Collaboration, 2018, AJ, 156, 123

Downloaded from academic.oup.com/mnras/article/519/1/709/6849985 by Imperial College of Science Technology and Medicine user on 19 October 2026

Barger A. J., Cowie L. L., Sanders D. B., Fulton E., Taniguchi Y., Sato Y., Kawara K., Okuda H., 1998, Nature, 394, 248
Barger A. J., Wang W. H., Cowie L. L., Owen F. N., Chen C. C., Williams J. P., 2012, ApJ, 761, 89
Baugh C. M., Lacey C. G., Frenk C. S., Granato G. L., Silva L., Bressan A., Benson A. J., Cole S., 2005, MNRAS, 356, 1191
Béthermin M. et al., 2017, A&A, 607, A89
Blain A. W., Smail I., Ivison R. J., Kneib J. P., Frayer D. T., 2002, Phys. Rep., 369, 111
Bothwell M. S. et al., 2013, MNRAS, 429, 3047
Bradley L. et al., 2021, astropy/photutils: 1.3.0, Zenodo, available at https://doi.org/10.5281/zenodo.5796924
Brown R. L., Wild W., Cunningham C., 2004, Adv. Space Res., 34, 555
Bussmann R. S. et al., 2015, ApJ, 812, 43
Capak P. L. et al., 2011, Nature, 470, 233
Carilli C. L. et al., 2010, ApJ, 714, 1407
Casey C. M., 2016, ApJ, 824, 36
Casey C. M., 2020, ApJ, 900, 68
Casey C. M., Narayanan D., Cooray A., 2014, Phys. Rep., 541, 45
Casey C. M. et al., 2015, ApJ, 808, L33
Casey C. M. et al., 2018, ApJ, 862, 77
Casey C. M. et al., 2021, ApJ, 923, 215
Chapin E. L., Berry D. S., Gibb A. G., Jenness T., Scott D., Tilanus R. P. J., Economou F., Holland W. S., 2013, MNRAS, 430, 2545
Chapman S. C., Blain A. W., Smail I., Ivison R. J., 2005, ApJ, 622, 772
Cheng T. et al., 2019, MNRAS, 490, 3840
Chen C.-C. et al., 2015, ApJ, 799, 194
Clements D. L., Dunne L., Eales S., 2010, MNRAS, 403, 274
Clements D. L. et al., 2014, MNRAS, 439, 1193
Clements D. L. et al., 2016, MNRAS, 461, 1719
Cochrane R. K. et al., 2021, MNRAS, 503, 2622
Cook M., Barausse E., Evoli C., Lapi A., Granato G. L., 2010, MNRAS, 402, 2113
Cox P. et al., 2011, ApJ, 740, 63
Cunningham C. R., Gear W. K., Duncan W. D., Hastings P. R., Holland W. S., 1994, in Crawford D. L., Craine E. R., eds, Proc. SPIE Conf. Ser. Vol. 2198 , Instrumentation in Astronomy VIII. SPIE, Bellingham, p. 638
da Cunha E. et al., 2015, ApJ, 806, 110
Daddi E. et al., 2009, ApJ, 694, 1517
Danielson A. L. R. et al., 2017, ApJ, 840, 78
Dannerbauer H. et al., 2014, A&A, 570, A55
Davé R., Finlator K., Oppenheimer B. D., Fardal M., Katz N., Kereš D., Weinberg D. H., 2010, MNRAS, 404, 1355
Donevski D. et al., 2018, A&A, 614, A33
Dowell C. D. et al., 2014, ApJ, 780, 75
Dudzevičiūtė U. et al., 2020, MNRAS, 494, 3828
Duivenvoorden S. et al., 2018, MNRAS, 477, 1099
Economou F., Bridger A., Wright G. S., Jenness T., Currie M. J., Adamson A., 1999, in Mehringer D. M., Plante R. L., Roberts D. A., eds, ASP Conf. Ser. Vol. 172, Astronomical Data Analysis Software and Systems VIII. Astron. Soc. Pac., San Francisco, p. 11
Engel H. et al., 2010, ApJ, 724, 233
Farrah D. et al., 2006, ApJ, 641, L17
Fudamoto Y. et al., 2017, MNRAS, 472, 2028
García-Vergara C., Hodge J., Hennawi J. F., Weiss A., Wardlow J., Myers A. D., Hickox R., 2020, ApJ, 904, 2
Geach J. E. et al., 2017, MNRAS, 465, 1789
Gómez-Guijarro C. et al., 2019, ApJ, 872, 117
Greenslade J. et al., 2018, MNRAS, 476, 3336
Greenslade J., Clements D. L., Petitpas G., Asboth V., Conley A., Pérez-Fournon I., Riechers D., 2020, MNRAS, 496, 2315 (G20)
Greve T. R. et al., 2005, MNRAS, 359, 1165
Griffin M. J. et al., 2010, A&A, 518, L3
Gruppioni C. et al., 2013, MNRAS, 432, 23
Gruppioni C. et al., 2015, MNRAS, 451, 3419
Hainline L. J., Blain A. W., Smail I., Alexander D. M., Armus L., Chapman S. C., Ivison R. J., 2011, ApJ, 740, 96
Hayward C. C. et al., 2021, MNRAS, 502, 2922
Hill R. et al., 2018, MNRAS, 477, 2042
Hill R. et al., 2020, MNRAS, 495, 3124
Holland W. S. et al., 2013, MNRAS, 430, 2513
Hopkins P. F., Hernquist L., Cox T. J., Kereš D., 2008, ApJS, 175, 356
Ho P. T. P., Moran J. M., Lo K. Y., 2004, ApJ, 616, L1
Hughes D. H. et al., 1998, Nature, 394, 241
Ivison R. J. et al., 2012, MNRAS, 425, 1320
Ivison R. J. et al., 2016, ApJ, 832, 78
Jones L. H., Rosenthal M. J., Barger A. J., Cowie L. L., 2021, ApJ, 916, 46
Kartaltepe J. S. et al., 2012, ApJ, 757, 23
Kneissl R. et al., 2019, A&A, 625, A96
Koprowski M. P., Dunlop J. S., Michałowski M. J., Cirasuolo M., Bowler R. A. A., 2014, MNRAS, 444, 117
Kovács A., Chapman S. C., Dowell C. D., Blain A. W., Ivison R. J., Smail I., Phillips T. G., 2006, ApJ, 650, 592
Lee N. et al., 2013, ApJ, 778, 131
Liu H. B. et al., 2018, A&A, 612, A54
Ma J. et al., 2019, ApJS, 244, 30
MacKenzie T. P. et al., 2017, MNRAS, 468, 4006
Magnelli B. et al., 2012, A&A, 548, A22
Marrone D. P. et al., 2018, Nature, 553, 51
McMullin J. P., Waters B., Schiebel D., Young W., Golap K., 2007, in Shaw R. A., Hill F., Bell D. J., eds, ASP Conf. Ser. Vol. 376, Astronomical Data Analysis Software and Systems XVI. Astron. Soc. Pac., San Francisco, p. 127
Michałowski M. J. et al., 2017, MNRAS, 469, 492
Michałowski M. J., Dunlop J. S., Cirasuolo M., Hjorth J., Hayward C. C., Watson D., 2012, A&A, 541, A85
Miller T. B. et al., 2018, Nature, 556, 469
Montaña A. et al., 2021, MNRAS, 505, 5260
Oliver S. J. et al., 2012, MNRAS, 424, 1614
Oteo I. et al., 2017, preprint (arXiv:1709.04191)
Oteo I. et al., 2018, ApJ, 856, 72
Pantoni L. et al., 2021, MNRAS, 504, 928
Riechers D. A. et al., 2013, Nature, 496, 329
Riechers D. A. et al., 2017, ApJ, 850, 1
Riechers D. A. et al., 2021, ApJ, 907, 62
Rowan-Robinson M. et al., 2018, A&A, 619, A169
Sault R. J., Teuben P., Wright M. C. H., 2011, Astrophysics Source Code Library, recordascl:1106.007
Simpson J. M. et al., 2014, ApJ, 788, 125
Smail I., Ivison R. J., Blain A. W., 1997, ApJ, 490, L5
Smail I., Ivison R. J., Blain A. W., Kneib J. P., 2002, MNRAS, 331, 495
Smith D. J. B., Hayward C. C., Jarvis M. J., Simpson C., 2017, MNRAS, 471, 2453
Stach S. M. et al., 2019, MNRAS, 487, 4648
Strandet M. L. et al., 2016, ApJ, 822, 80
Swinbank A. M., Smail I., Chapman S. C., Blain A. W., Ivison R. J., Keel W. C., 2004, ApJ, 617, 64
Swinbank A. M. et al., 2014, MNRAS, 438, 1267
Tacconi L. J. et al., 2006, ApJ, 640, 228
Tacconi L. J. et al., 2008, ApJ, 680, 246
Targett T. A. et al., 2013, MNRAS, 432, 2012
Taylor M. B., 2005, in Shopbell P., Britton M., Ebert R., eds, ASP Conf. Ser. Vol. 347, Astronomical Data Analysis Software and Systems XIV. Astron. Soc. Pac., San Francisco, p. 29
Toft S. et al., 2014, ApJ, 782, 68
Umehata H. et al., 2015, ApJ, 815, L8
Walter F. et al., 2012, Nature, 486, 233
Wang T. et al., 2016, ApJ, 828, 56
Wang G. et al., 2021, MNRAS, 508, 3754
Wang W.-H. et al., 2017, ApJ, 850, 37
Wardlow J. L. et al., 2011, MNRAS, 415, 1479
Wilkinson A. et al., 2017, MNRAS, 464, 1380

Downloaded from academic.oup.com/mnras/article/519/1/709/6849985 by Imperial College of Science Technology and Medicine user on 19 October 2026

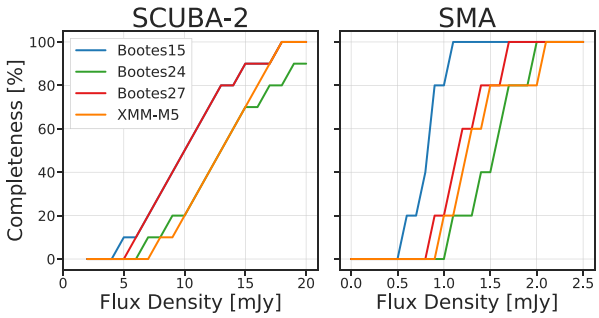


Figure A1. The completeness estimates for the SCUBA-2 maps (*left*) and SMA maps (*right*) associated with our four 500 μm risers. We find that in the SCUBA-2 maps, Bootes15 and Bootes27 reach a completeness of ∼50 per cent at 10 mJy, and rise to a completeness of ∼80 per cent at 14 mJy. Bootes24 and XMM-M5 reach an ∼80 per cent completeness at 17 and 16 mJy, respectively. For the SMA maps, Bootes15 reaches 80 per cent completeness at 1 mJy and 100 per cent at 1.1 mJy. Bootes24 and Bootes27 reach 80 per cent completeness at 1.7 and 1.4 mJy, respectively, while XMM-M5 reaches 80 per cent completeness at 2 mJy.

APPENDIX A: COMPLETENESS

In this section, we discuss the details of our completeness calculation for the SMA and SCUBA-2 maps. For each of our SCUBA-2 maps, we inserted fake sources within the 700 arcsec diameter circular region, where each fake source was defined as a simple 2D Gaussian with a random position, a defined peak flux density, and a width corresponding to $\sigma = 6.2$ arcsec (based on the 14.6 arcsec FWHM of the SCUBA-2 850 μm beam). We reran the source extraction method outlined in Section 4.3.1 on the map, counted the recovered fake sources, and hence calculated the completeness. For each run, we included 10 fake sources, all with the same peak flux density, and repeated the process 1000 times for each peak flux density value, starting from 2 mJy and increasing in steps of 1 mJy up to 20 mJy. The final completeness value for each source and peak flux density value is simply the median of the completeness distribution from the 1000 runs.

For the SMA completeness calculations, we take a slightly different approach. Given the smaller map size, we only include five fake sources in each iteration. Additionally, rather than modelling a symmetric 2D Gaussian with a defined width, we create a Gaussian kernel matching the beamshape of the observations as defined in the header information. We similarly complete 1000 iterations, inserting sources into the dirty maps with peak flux densities ranging from 0 to 2.5 mJy in steps of 0.1 mJy, and extracting sources with peak flux densities above the detection threshold for each map (see Section 3.1). The final completeness value for each map and peak flux density value is simply the median of the completeness distribution from the 1000 runs.

In Fig. A1, we present the result of these completeness calculations. For the SCUBA-2 maps, Bootes15 and Bootes27 both reach a completeness of ∼50 per cent at ∼10 mJy, and rise to a completeness of $\gtrsim$ 80 per cent at 14 mJy. Bootes24 and XMM-M5 have a poorer completeness, reaching ∼80 per cent at ∼17 and ∼16 mJy, respectively. For the SMA maps, Bootes15 reaches 100 per cent completeness at 1.1 mJy. Bootes24 and Bootes27 reach 50 per cent completeness at 1.6 and 1.2 mJy, 80 per cent at 1.9 and 1.4 mJy, and up to 100 per cent at 2 and 1.7 mJy, respectively. Finally, XMM-M5 performs quite well at low flux densities, reaching 50 per cent completeness at 1.3 mJy, but does not reach 100 per cent completeness until 2.1 mJy.

APPENDIX B: SCUBA-2 MAPS

In Fig. B1, we present the full SCUBA-2 signal-to-noise maps at 850 μm for the fields covering our four 500 μm risers. These maps were reduced using the `REDUCE_SCAN_FAINT_POINT_SOURCES` recipe, and sources were extracted within the white dashed circle. We note that the SMGs are distributed differently within the different fields. Sources in Bootes15 are mostly clustered towards the South Western region of the map, while sources in Bootes27 seem to be more clustered around the centre. Sources in Bootes24 and XMM-M5 are more spread out across the map.

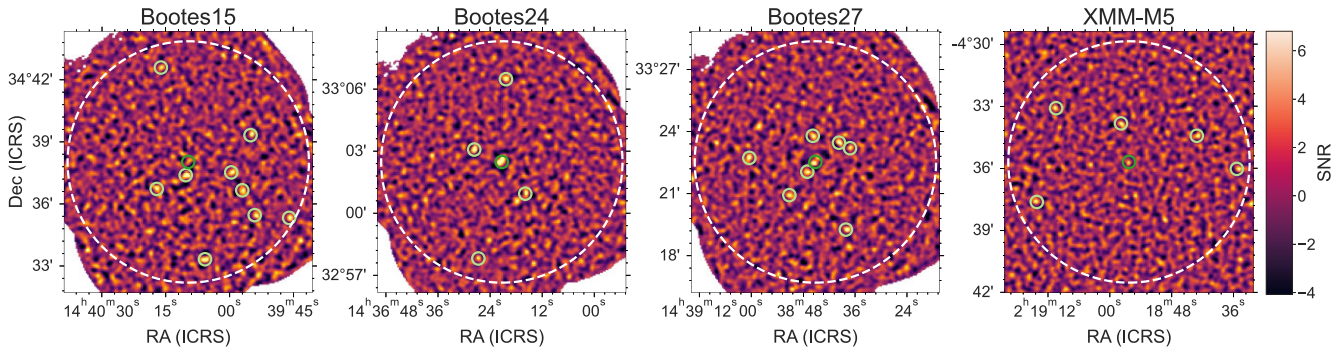


Figure B1. SCUBA-2 signal-to-noise maps at 850 μm centred on each of our 500 μm risers reduced using the `REDUCE_SCAN_FAINT_POINT_SOURCES` recipe. The darker circles show the positions of the 500 μm risers, while the lighter circles show the positions of the SNR > 4 detected SCUBA-2 sources. The white dashed line shows the circle of radius 350 arcsec over which sources are extracted.

Downloaded from academic.oup.com/mnras/article/519/1/709/6849985 by Imperial College of Science Technology and Medicine user on 19 October 2026

APPENDIX C: *HERSCHEL* SPIRE AND SCUBA-2 COMPARISON

In Fig. C1, we compare the *Herschel* SPIRE and SCUBA-2 850 μm maps to investigate the effects of blending on the observed photometry of our four 500 μm risers. We find little evidence of artificial reddening in Bootes24 and XMM-M5, with no nearby detections in the SCUBA-2 maps, and all potential 250 μm sources detected as separate objects in the HerMES catalogue, indicating that their flux densities have been deblended. For Bootes15, there is a second SNR > 4 SCUBA-2 detection within the *Herschel* SPIRE 500 μm beamsize, which is bright at 850 μm but is faint enough at 250 μm to remain undetected in the HerMES catalogue. We similarly find an SNR > 4 SCUBA-2 detection less than ≈30 arcsec South East of Bootes27 that remains undetected in the HerMES catalogue.

We make a simple estimate of the likely effect of these contaminating sources on the 350 and 500 μm flux densities of Bootes15 and Bootes27. We first extract a simple flux density estimate at 250 μm for the contaminating sources, using the peak flux density within the SPIRE beamsize centred on the brightest pixel in the SCUBA-2 850 μm maps. We conservatively estimate the likely peak flux of these contaminating sources by linearly interpolating between their 250 μm flux densities and their deboosted 850 μm flux densities. In each of the 350 and 500 μm bands, we construct a Gaussian function with a peak matching the interpolated flux density, and an FWHM matching the beamsize of the SPIRE instrument in that band. Finally, based on these Gaussians, we estimate the likely contaminating flux

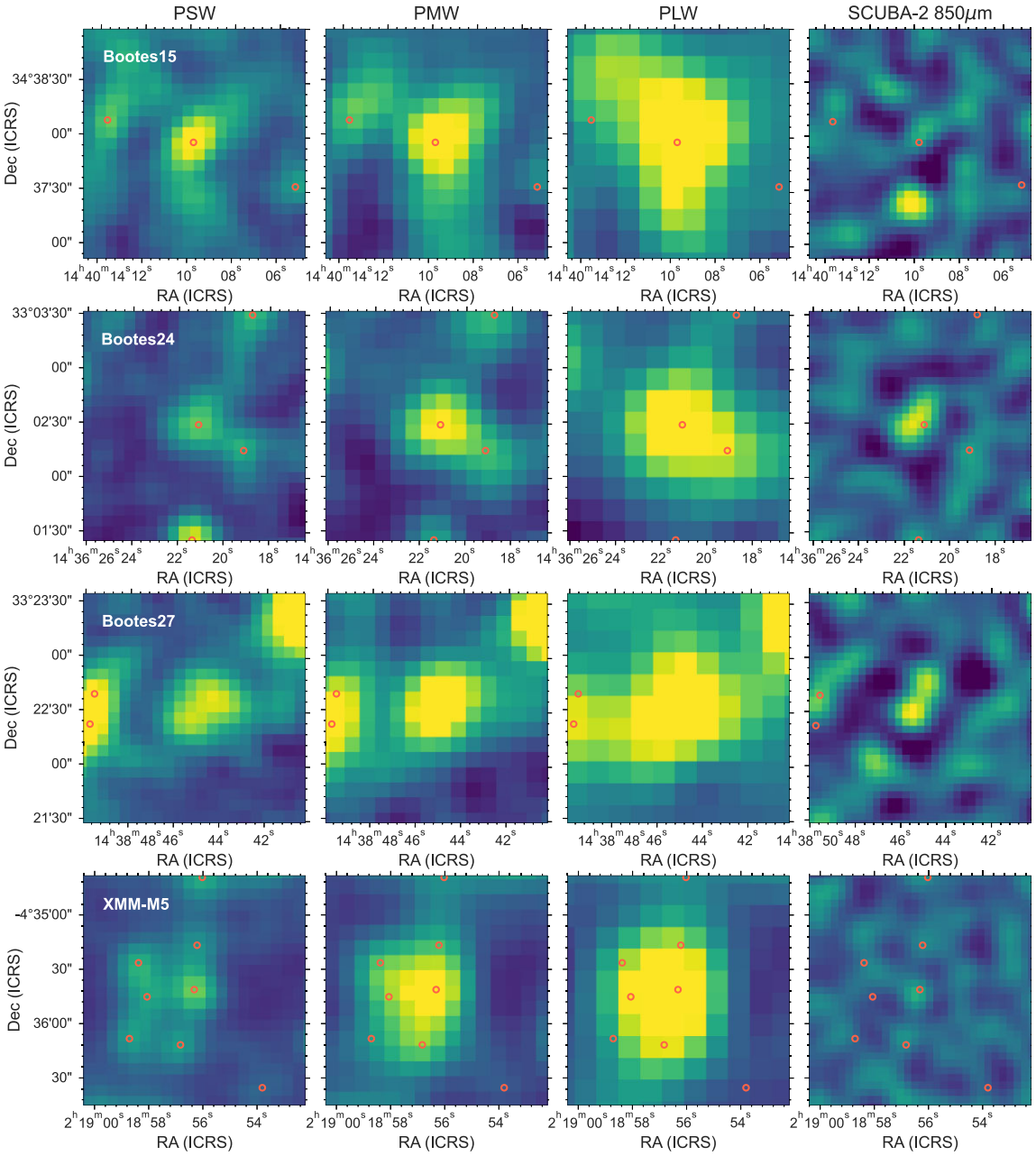


Figure C1. Comparison of the *Herschel* SPIRE maps (where PSW, PMW, and PLW refer to the 250, 350, and 500 μm bands, respectively) and their SCUBA-2 850 μm point source maps from this study. Plotted as red points are the positions of 250 μm-selected sources from the HerMES catalogue.

Downloaded from academic.oup.com/mnras/article/519/1/709/6849985 by Imperial College of Science Technology and Medicine user on 19 October 2026

at the position of the brightest pixel in the *Herschel* SPIRE images at 350 and 500 μm. We find that the contaminating source associated with Bootes15 could conservatively contribute ∼1.1 and ∼3.6 mJy at 350 and 500 μm, respectively, well within the quoted errors for the *Herschel* SPIRE flux density in these bands. The contamination for Bootes27 is similarly small, ∼0.3 and ∼2.8 mJy at 350 and 500 μm, respectively. We subtract these potential contaminating flux densities and rerun the resulting photometry through MMPZ, finding that it makes no appreciable difference to the estimated photometric redshifts within their associated errors.

APPENDIX D: PROBABILITY DENSITY FUNCTIONS

In Fig. D1, we present the photometric redshift PDFs obtained from MMPZ for our 500 μm risers and the other SNR > 4 detections in the SCUBA-2 fields. The MMPZ fitting algorithm finds the most likely redshift at which a galaxy resides by determining where its FIR/mm SED is most consistent with the observed $L_{\rm IR}$–$\lambda_{\rm peak}$ relation, where $\lambda_{\rm peak}$ is the rest-frame wavelength at which the FIR/mm SED peaks (Lee et al. 2013; Strandet et al. 2016; Casey et al. 2018, 2021; Casey 2020). We find that the photometric redshifts for Bootes15, Bootes15.SCUBA1, and Bootes15.SCUBA2 are poorly constrained due to poor-quality photometry. By comparison, we find that the photometric redshift PDFs for the sources in the Bootes24 field are all well constrained, likely residing at redshifts of $z \sim 2$–3, with Bootes24 itself being somewhat broader with a higher redshift tail to its PDF. For Bootes27 and XMM-M5, the photometric redshift PDFs are similarly well constrained, but the sources are spread over a wider range of redshifts, with two of the SCUBA-2 sources likely residing at $z \sim 2$, one likely residing at $z \sim 4$, and XMM-M5 itself straddling these two redshifts. For Bootes24, Bootes27, and XMM-M5, these results are in good agreement with the FIR/sub-mm colours shown in Fig. 8. We additionally include the full photometric PDFs for each of the SMA components associated with Bootes15 and Bootes24, and for the two partially resolved SCUBA-2 sources associated with Bootes27, after the simple deblending outlined in Section 4.2, although we note that these are exceedingly similar to the photometric redshift PDFs for the total 500 μm riser systems.

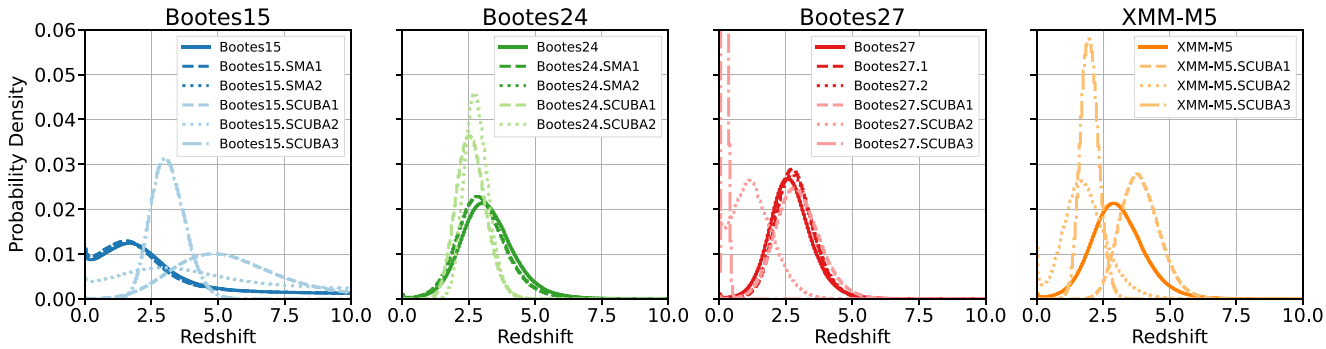


Figure D1. Normalized photometric redshift PDFs for our 500 μm risers and their associated SNR > 4 SCUBA-2 detections estimated by MMPZ.

This paper has been typeset from a TEX/LATEX file prepared by the author.

Downloaded from academic.oup.com/mnras/article/519/1/709/6849985 by Imperial College of Science Technology and Medicine user on 19 October 2026